5-2018

Diffraction of Laguerre Gaussian Vortex Beams

Anindya Ambuj
University of Arkansas, Fayetteville

Diffraction of Laguerre Gaussian Vortex Beams

A dissertation submitted in partial fulfillment
of the requirements for the degree of
Doctor of Philosophy in Physics

by

Anindya Ambuj
Loyola College
Bachelor of Science in Physics 2008
Pondicherry University
Master of Science in Physics, 2010
University of Arkansas
Master of Science in Physics, 2015

May 2018
University of Arkansas

This dissertation is approved for recommendation to the Graduate Council.

Surendra Singh, Ph.D.
Dissertation Director

Reeta Vyas, Ph.D.
Committee Member

Salvador Barraza-Lopez, Ph.D.
Committee Member

Min Xiao, Ph.D.
Committee Member

Brajendra Panda, Ph.D.
Committee Member

Abstract

The natural phenomenon of waves bending around obstacles is diffraction. Spatial characteristics of the diffraction pattern depends on the incident wave field, the shape, and size of the aperture. The diffraction of a plane wave of light by a slit and a circular aperture produce the sinc-squared and the Airy intensity patterns, respectively. On the contrary, the diffraction of Laguerre-Gauss vortex (LGV) beams by simple apertures such as a slit, circular apertures, and polygons show many unexpected features.

LGV beams have $\rho^{\ell}e^{i\ell\phi}$ transverse spatial dependence, where ρ is the distance from the beam axis, ϕ the azimuthal angle, and ℓ is the index of orbital angular momentum that corresponds to $\ell\hbar$ of orbital angular momentum per photon. The LGV beams were produced from Hermite-Gauss beams using an astigmatic mode converter. The LGV beams were diffracted by a slit, circular apertures, and polygons. The far-field diffraction pattern was recorded.

LGV beam of order ℓ when diffracted by a slit at the beam waist showed, $\ell + 1$ fringes. The diffraction performed along the direction of propagation, away from the waist, showed a shear in the pattern, with maximum shear at Rayleigh range. As the slit was moved even further away, the diffraction pattern evolved into two dominant peaks irrespective of ℓ. When LGV beams of order ℓ are diffracted by a circular aperture, the minima of the diffracted field depend on the zeros of $\ell + 1$ order Bessel functions. The center of the diffraction pattern has a minimum for $\ell \geq 1$. When the beam axis and the aperture axis are laterally separated, this central minimum splits into ℓ minima. The diffraction of LGV beams by regular polygons created an optical lattice. The diffraction pattern by a regular

polygon of n sides has $n-$fold symmetry for both even and odd n, unlike the $2n-$fold symmetry for odd n, and $n-$fold for even n due to a plane wave. The center of the diffraction pattern is bright for $\ell = n$, and multiples of n. The diffraction pattern has a repeating, nesting structure for $\ell > n$. The experimental results are in good agreement with the theoretical predictions.

Acknowledgements

I have many people to thank for making my experience as a graduate student pursuing a doctoral degree in physics truly rewarding. This would not be possible without the help and support of the kind, helpful and professional physics department staff. Thank you.

Each of the members of my Dissertation Committee has provided me extensive professional and personal guidance. I would especially like to thank Dr. Surendra Singh. As my teacher and mentor, he has taught me more than I could ever give him credit for here. He has shown me, by his example what a good scientist (and person) should be. He always encouraged me to be thorough. I am deeply grateful of your patience with me, and your open door policy to meet with students. You were always present when I wanted to meet you. I would like to thank Dr. Vyas, for the hours of discussions, and introducing me to world of numerical modeling. Ann and me will also be eternally grateful for your moral support and advice when things were a little dicey.

I would like to thank Sean, for not only being a very good and supporting friend, but also for teaching me and helping me use the SLM. I would also like to thank Bala, Hemlin, Venkat, Shasvath, Kevin and many more physics graduate students for hours of intersting discussions and debates.

Thank you my dearest Ann, for withstanding my eccentricities and being there with me through thick and thin. I am very lucky to have found one of the best people in the world as my soulmate. Thank you my dear son, Ashankit, your smile brought hope and kept me going. I would like to thank Linu, for being the best sister ever. I am eternally grateful to my mother in law, whose help at crucial times helped us tremendously. I would like to

thank Dr. Brajendra Panda, and Ms. Rashimi Panda for being there for us through thick and thin. Your incredible support made us feel at home, away from home.

And finally, I would like to express my most heartfelt gratitude to Mama and Papa, your guidance is invaluable. You have been the untiring lighthouse every moment of my life, and know me better than anyone else.

Contents

List of Figures

Chapter 1

Intoduction

The natural phenomenon of waves bending around obstacles is called diffraction. The diffraction pattern depends on the geometry of the obstacle and the incident wave field. Some obstacles, like apertures are present in most scientific light detecting devices, for example, cameras have polygonal apertures, and circular apertures.

The interaction of light with apertures has been of interest at least for the last four hundred years. Some of the earliest work was done by a Jesuit priest, Francesco Grimaldi in the 1600s [1], who coined the term 'diffraction'. He observerd that when light passes through a hole it takes the form of a cone. If light took a rectilinear path then this phenomenon could not be described. Isaac Newton built upon Grimaldi's observations when he encountered diffraction bands [2]. The diffraction patterns due to feathers were first recorded by James Gregory [3], which acted as a diffraction grating. In 1803, Thomas Young perfomed his famous double slit experiment [4] and around the same time Augustin-Jean Fresnel studied the effects of diffraction [5] in great detail giving experimental support to Christiaan Huygens' wave theory [6].

The development of lasers and its applications in the 1960s and 1970s [7–9] reinvigorated the interest in diffraction. The study of Hermite-Gauss (HG) laser beams were conducted in detail through 1980s [10, 11]. Most laser beams used today for comercial applications are HG laser beams. Though this is quickly changing in the telecommunication sector [12].

The Hermite-Gauss and Laguerre-Gauss modes are beam solutions to the scalar

Helmholtz equations in the paraxial limit [8, 9, 13]. An approach to solving these is briefly discussed in the diffraction section. In the 1990s, methods to create the Laguerre-Gaussian (LG) laser beams were invented [14–16]. These beams had orbital angular momentum in addition to the spin angular momentum that each photon carries. The study of LG beams had begun.

In early 2010s the study of the diffraction properties of the LG beams were underway [17–22]. The LG beams have cylindrical symmetry. Laguerre-Gauss Vortex (LGV) beams are a sub-catagory of the LG beams. The LGV beams when projected onto a screen look like a ring or a donut. This led to their less formal but affectionate name of the donut beams [23, 24].

In this study we describe the diffraction of these Laguerre-Gauss vortex laser beams by apertures of different shapes. In the subsequent sections of this chapter we take a closer look at some concepts in diffraction of light, and review the method used in the production of Laguerre-Gauss vortex beams of various sizes.

1.1 Diffraction

To obtain a model for diffraction of light by an aperture in air, we assume the medium is homogeneous and non-dispersive so that k is constant. We also assume the use of a monochromatic scalar wave $\psi(x)e^{-i\omega t}$ with its spatial part satisfying Helmholtz equation

$$\left(\nabla^2 + k^2\right)\psi = 0. \tag{1.1}$$

Here $k = 2\pi/\lambda$ is the wave number and ω is the angular frequency of light. For a wave travelling in vaccuum, $k = \omega/c$.

The solution of the Helmholtz equation inside a volume is completely determined by the value of ψ and its normal derivative on the boundary. There is a nice mathematical approach to solving this by the use of Green's theorem. Inspecting $\psi_0 = e^{ikr}/r$ as a solution, this approach leads to the Kirchhoff integral. The details of Kirchhoff integral can be found in Chapter 3 of [25] and Chapter 8 of [26].

Diffraction of light waves by such a model can be classified into two broad categories. The Fresnel diffraction, and the Fraunhofer diffraction. The Fresnel or near-field diffraction, as the name suggests, is used to describe the diffraction pattern produced by waves that pass through an aperture or around an obstacle usually when viewed relatively close to the obstacle. If d is the distance of the observation point from the obstacle, a the size of the obstacle or aperture, and λ the wavelength of the wave that is incident on the obstacle, then a region where $\sqrt{\lambda d} \ll a$ is called the Fresnel region.

The Fraunhofer diffraction, on the other hand, is known as the far-field diffraction. In contrast to Fresnel diffraction, the diffraction pattern is observed far away from the aperture. The condition here is $\sqrt{\lambda d} \gg a$. In most laboratory situations placing an observation screen or a camera far away can be an inconvenience, and in some situations the intensity of light would have diminished so significantly that such observations cannot be recorded with a high signal to noise ratio. This problem can be overcome by realizing that the amplitude of the Fraunhofer diffraction pattern is given by the 2D Fourier transform of the aperture function [25]. One of the many remarkable and useful properties of a converging lens is its ability to perform a 2D Fourier transform. When the input is in the front focal plane of the lens and the output is recorded at the back focal plane, the phase curvature introduced due to the lens disappears, leaving an exact 2D Fourier

transform relation. Chapter 5 in [25] goes over this in detail. In our experiment the aperture is in the front focal plane of a lens and the camera is in the back focal plane of the same lens, thus recording a 2D Fourier transform or the Fraunhofer diffraction pattern of the aperture. This arrangement is referred to as the '$2f$' arrangement.

1.2 Laguerre Gauss Beams

One of the beam solutions of the Maxwell's wave equation is the Laguerre Gaussian beam [8, 9, 13, 27], which in the cylindrical coordinates propagating along the z direction has the form

$$u(\rho,\phi,z) = \frac{C_{\ell p}^{LG}}{w}\left(\frac{\sqrt{2}\rho}{w}e^{i\phi}\right)^{|\ell|} L_p^{|\ell|}\left(\frac{2\rho^2}{w^2}\right) \times \exp\left(-\frac{\rho^2}{w^2}\left(1 - i\frac{z}{z_R}\right) + ikz - iN\theta(z)\right), \tag{1.2}$$

where $C_{\ell p}^{LG}$ is a constant, L_p^{ℓ} are the generalized Laguerre polynomials, ρ is the radial distance of a point from the beam axis, k is the wave number, $N = |\ell| + 2p$, $z_R = kw_0^2/2$ is the Rayleigh range, $w = w_0[1 + z^2/z_R^2]^{1/2}$ is the beam spot size with minimum value w_0 at the waist, and $\theta(z) = tan^{-1}[z/z_R]$ is Guoys phase of the beam.

The LG beam can be created in the laboratory. One of the first methods to create these LG beams involved conversion of Hermite gauss beams to Laguerre Gauss beams [14, 23]. The same method is used for our experiments.

The process of creating LG beams starts with the creation of HG modes, with an open laser cavity. In our case the laser cavity had one spherical mirror and a plane mirror was used as the output mirror. Between the Brewster window and the output mirror there are

two thin crossed silk fibers. If the direction of propagation is along the z axis, then to choose the HG modes, the fibers are moved in the x and y direction creating loss in particular spots thus allowing only certain HG modes to oscillate. The choice of a plane mirror as the output mirror of the laser cavity forces the waist of the laser beam on the plane mirror. This set up is shown in Figure 1.1.

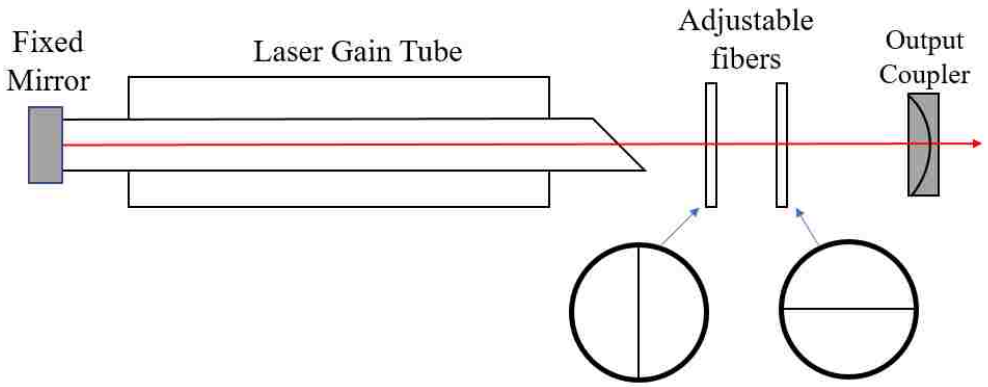

Figure 1.1: A schematic diagram showing the crossed fibers after the brewster's window, but before the output mirror, used to create various HG modes.

After the creation of the HG modes, these modes are focused to a waist using a lens L_1 of focal length f_1. These HG modes are converted to the LG modes, using a pair of cylindrical lenses. These cylindrical lenses have been turned 45° about the axis and are placed such that they are on either side of the focus of lens L_1 symetrically. The spacing of the cylindrical lens is $\sqrt{2}f$, where f is the focal length of the cylindrical lens. In a cylindrical lens, one component of the input beam sees a lens and is focused to a waist and expands again. Thus undergoing a Gouy's phase change of π, whereas the other component sees a glass plate. Thus creating an astigmatism. The second cylindrical lens is used for phase matching by creating another astigmatism. This arrangement of the two cylindrical lens is known as the $\pi/2$ mode converter or an astigmatic mode converter. The beam that

comes out of the mode converter is an LG beam. This set up is shown in Figure 1.2.

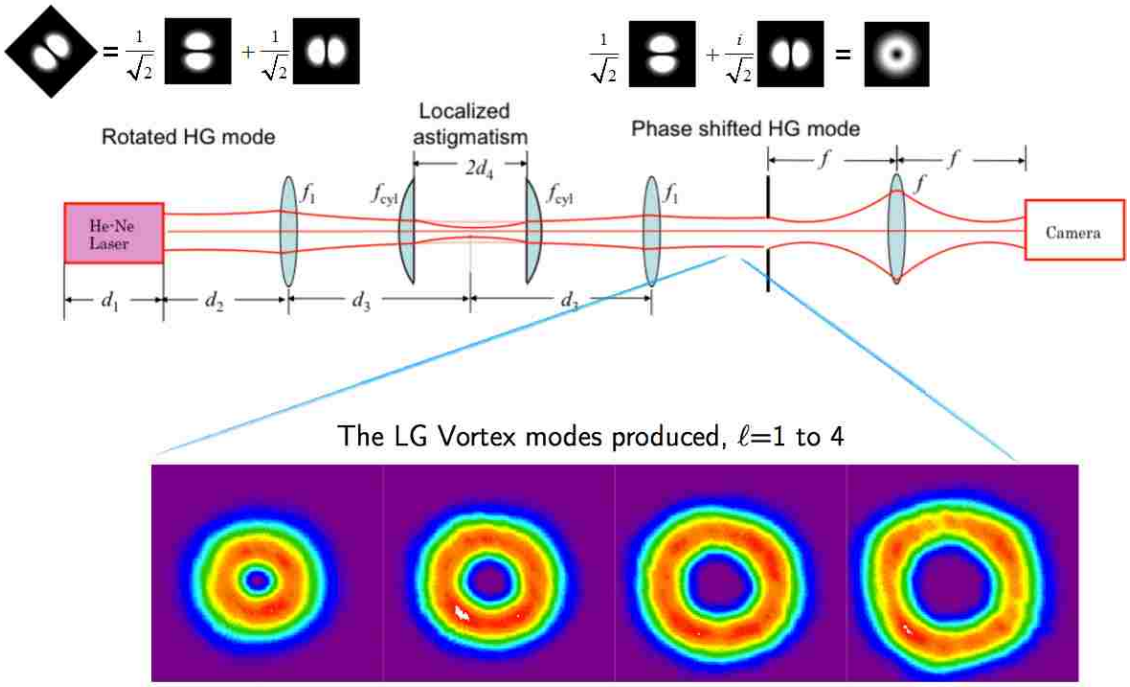

Figure 1.2: A schematic diagram of the experimental set up and the LGV modes produced using the set up for $\ell = 1 - 4$.

The size of this LG beam can be controlled by adding lenses after the mode converter. As seen in Figure 1.3, let w_{01} be the first waist before the lens, let the waist be a distance d_1 from the lens, w_{02} be the waist after the beam has passed through a lens of focal length f, and is formed a distance d_2 from the lens, then w_{02} and d_2 can be calculated using the matrix method of beam propagation for a gaussian beam. The final results of this calculations are

$$w_{02} = \frac{w_{01}}{\sqrt{(z_1/f)^2 + (1 - d_1/f)^2}}, \qquad d_2 = \frac{(z_1^2/f) - d_1(1 - d_1/f)}{(z_1/f)^2 + (1 - d_1/f)^2}, \tag{1.3}$$

where $z_1 = \pi w_{01}^2/\lambda$ is the Rayleigh range before light passes through the lens. The beams of interest in this study is the Laguerre Gauss Vortex (LGV) beam. The LGV beam is a

LG beam with zero radial index. That is, in Equation 1.2, we substitute $p = 0$.

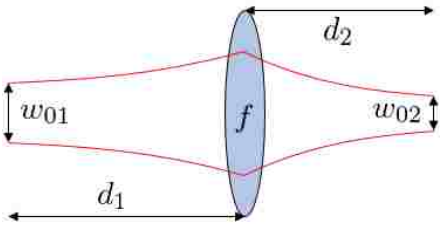

Figure 1.3: A schematic diagram of a single lens used to change the waist size from w_{01} to w_{02}.

Chapter 2

Single Slit Diffraction

2.1 Introduction

Diffraction of LGV beams with simple apertures exhibit unexpected novel features. Most experiments so far have focused on the role of azimuthal variation of phase, of the incident beam, in the plane of the aperture [17, 19–21, 28, 29]. An integral part of LGV beams, the effect of quadratic radial dependence of phase in the plane of the aperture, has not been explored till now. The curvature of the incident phase front is caused by this quadratic radial variation of the phase and adds another element that governs the diffraction pattern of LGV beams. We find that in the waist region, quadratic radial variation of phase in the plane of the diffracting slit causes a shear of the diffraction pattern even when the slit is centered on the beam. Beyond this region, phase front curvature leads to significant modifications of the diffraction pattern. We present a closed form analytical expression for the diffracted field, valid for a centered slit whose aperture axis coincides with the beam axis, which can account for the experimentally recorded diffraction profiles well for all slit locations relative to the incident beam waist along the beam axis. We begin with an analytic description of the new features expected in the Fraunhofer diffraction of an LGV beam by a long slit. This is followed by a description of the experimental set-up to observe these new features. This chapter ends with a discussion of the experimental results which are in good agreement with the theoretical results.

Consider a two-dimensional aperture A in an opaque plane screen occupying the $x'y'$ plane illuminated by a field propagating in $+z$ direction. Let $U_{in}(x', y', z)$ be the incident

field in the plane of the aperture. Then the diffracted field in the far zone (Fraunhofer diffraction) is proportional to the Fourier transform of the incident field distribution in the plane of the aperture.

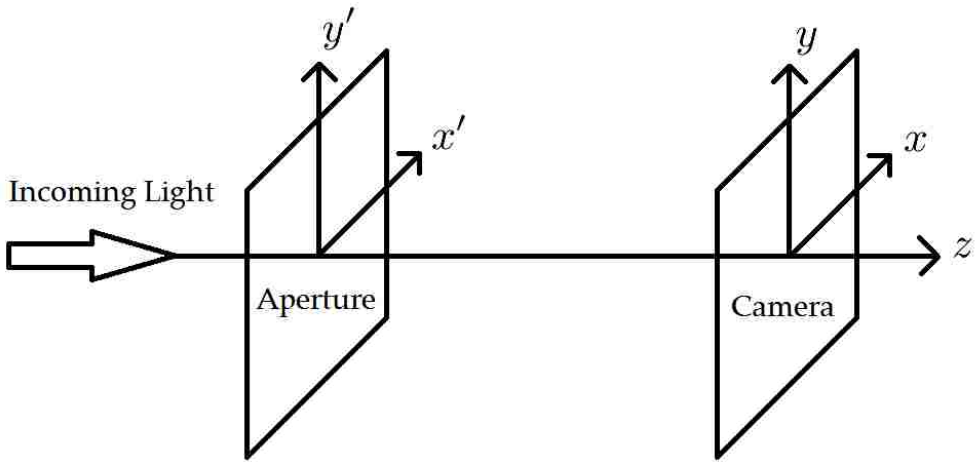

Figure 2.1: The geometry of the incoming light and the cartesian coordinates of the aperture plane and the image plane.

This same field pattern will be obtained if the aperture is located in the front focal plane of a lens of focal length f, and then the diffracted field is observerd in the back focal plane of the lens [25]. This is called the 2f-geometry to observe Fraunhofer diffraction by an aperture. In this case the diffracted field in the back focal plane of the lens is given by

$$U_f(x,y) = \frac{ik}{2\pi f} \iint_A dA U_{in}(x',y',z) \times \exp\left[-\frac{ik}{f}(xx'+yy')\right], \tag{2.1}$$

where $k = 2\pi/\lambda$ is the wavenumber, λ is the wavelength of light, and z is the location of the aperture along the beam axis and x, y are the transverse coordinates of a point in the observation plane (back focal plane of the lens). Equation 2.1 expresses the fact that the diffracted field is the Fourier transform of the incident field limited by the aperture.

If U_{in} is a plane wave, and the diffraction takes place at a single slit of width d and

height b, then the diffracted field intensity is given by

$$I(x,y) = C\left[\frac{\sin\beta}{\beta}\right]^2\left[\frac{\sin\delta}{\delta}\right]^2, \tag{2.2}$$

where $\beta = kbx/2f$ and $\delta = kdy/2f$ are dimensionless variables, which may be thought of as scaled cartesian coordinates for the diffraction plane. Figure 2.2 shows the diffraction pattern for a slit that is oriented vertically when illuminated by a plane wave.

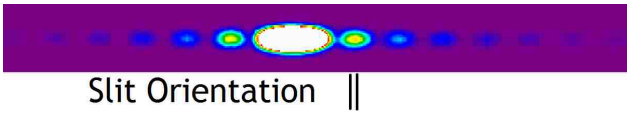

Figure 2.2: Diffraction of a plane wave by a single slit

The field of LGV beams has $\rho^\ell e^{i\ell\phi}$ transverse spatial dependence, and the diffraction pattern of LGV beams by a slit is different from that of the plane wave. This is explored in detail in the subsequent sections.

2.2 Theory

We consider LGV beams as LG beams with zero radial index as described in chapter 1. For an incident LGV beam the incident field in the plane of the aperture is of the form

$$U_{in}(x',y',z) = C_\ell\left(\frac{\sqrt{2}\rho'}{w}e^{i\phi'}\right)^\ell \times e^{-\frac{\rho'^2}{ww_0}\left(1-i\frac{(z-z_0)}{z_R}\right)+ik(z-z_0)-i(\ell+1)\theta(z)}, \tag{2.3}$$

where $\rho' = (x'^2+y'^2)^{1/2}$ is the radial distance of a point in the aperture A from the beam axis, z_0 is the location of the incident beam waist, $z_R = kw_0^2/2$ is the Rayleigh range, $w(z) = w_0[1+(z-z_0)^2/z_R^2]^{1/2}$ is the beam spot size with minimum value w_0 at the waist, and $\theta(z) = tan^{-1}[(z-z_0)/z_R]$ is Guoys phase of the beam. In Equation 2.3 we have expressed the radius of curvature of the incident beam $R(z)$ in terms of $w(z)$ as

$R(z) = [kz_R/2(z - z_0)]w^2$. The phase of the incident beam can also be written as $\ell\phi' + k\rho'^2/2R(z) + k(z - z_0) - (\ell + 1)\theta(z)$, where the first term describes azimuthal variation of the phase which results in the helical twist of the phase front and the second term describes a quadratic radial variation of phase due to curvature of the phase front [8, 9].

Equation 2.3 is written for LGV beams with a positive topological charge ℓ. It also holds for LGV beams of negative topological charge if ℓ is taken as the magnitude of the charge and $\exp(i\phi')$ is replaced by $\exp(-i\phi')$. The diffracted field in the Fraunhofer limit is then given by

$$U_f^\ell(x, y) = C'_\ell \iint_A dA \left(\frac{\sqrt{2}\rho'}{w} e^{i\phi'}\right)^\ell \times \exp\left[-\frac{\rho'^2}{ww_0}\exp[-i\theta(z)] - \frac{ik}{f}(xx' + yy')\right], \quad (2.4)$$

where the factors independent of the variables of integration including $\exp[-i(\ell + 1)\theta(z) + ik(z - z_0)]$, have been absorbed into the constant C'_ℓ and $\left(1 - i\frac{(z-z_0)}{z_R}\right) = \exp[-i\theta(z)]$.

For a rectangular slit of length b ($-b/2 \le x \le b/2$) and width d ($-d/2 \le y \le d/2$), this integral can be cast in a more convenient form by introducing some new variables:

$$u = \frac{x'\exp(-i\theta/2)}{(ww_0)^{1/2}}; \quad v = \frac{y'\exp(-i\theta/2)}{(ww_0)^{1/2}};$$

$$u_0 = \frac{b\exp(-i\theta/2)}{2(ww_0)^{1/2}} = \mu\exp(-i\theta/2); \quad v_0 = \frac{d\exp(-i\theta/2)}{2(ww_0)^{1/2}} = \nu\exp(-i\theta/2);$$

$$\kappa_x = \frac{kx(ww_0)^{1/2}\exp(i\theta/2)}{f}; \quad \kappa_y = \frac{ky(ww_0)^{1/2}\exp(i\theta/2)}{f}. \quad (2.5)$$

Then the diffraction integral becomes

$$U_f(x, y) = C'_\ell(ww_0)\left[i\exp(-i\theta/2)\left(\frac{2w_0}{w}\right)^{1/2}\right]^\ell \times \left[\frac{\partial}{\partial\kappa_x} + i\frac{\partial}{\partial\kappa_y}\right]^\ell f_u(\kappa_x)f_v(\kappa_y), \quad (2.6)$$

where

$$f_u(\kappa_x) = \int_{-u_0}^{u_0} du \exp(-u^2 - i\kappa_x u),$$
$$= \frac{\pi^{1/2}}{2} \exp(-\kappa_x^2/4)[\mathrm{erf}(u_0 + i\kappa_x/2) + \mathrm{erf}(u_0 - i\kappa_x/2)]; \tag{2.7}$$

$$f_v(\kappa_y) = \int_{-v_0}^{v_0} dv \exp(-v^2 - i\kappa_y v)$$
$$= \frac{\pi^{1/2}}{2} \exp(-\kappa_y^2/4)[\mathrm{erf}(v_0 + i\kappa_y/2) + \mathrm{erf}(v_0 - i\kappa_y/2)]. \tag{2.8}$$

Here, erf(ξ) is the error function with complex argument ξ [30]. The diffracted field was evaluated by integrating Equation 2.4 numerically to obtain the theoretical diffraction patterns, which were later compared with the experimentally obtained patterns.

By considering the expression for the diffracted field in some simple but realistic limits, some insight into the diffraction pattern can be gained. Let's consider a long thin slit of length b large compared to the beam spot size ($b \gg w$, w_0) and width d small compared to the beam spot size w_0, we can evaluate the diffraction integrals in Equatoins 2.7 and 2.8 for LGV beams as

$$f_u \approx \int_{-\infty}^{\infty} du \exp(-u^2 - i\kappa_x u) = \pi^{1/2}\exp(-\kappa_x^2/4)$$
$$= \pi^{1/2} exp(-\beta^2/4v_0^2), \quad \beta = \frac{kbx'}{2f} \tag{2.9}$$

$$f_v \approx 2v_0 \frac{\sin\delta}{\delta}, \quad \delta = \frac{kdy}{2f}, \tag{2.10}$$

where v_0 is given by Equation 2.5. β and δ are real dimensionless variables, which may be thought of as scaled Cartesian coordinates for the diffraction plane. Substituting these

results in Equation 2.6,

$$U_f(x,y) = C'_\ell(ww_0)\left(i\exp(-i\theta/2)\left(\frac{2w_0}{w}\right)^{1/2}\right)^\ell \times \left(\frac{\partial}{\partial\kappa_x} + i\frac{\partial}{\partial\kappa_y}\right)^\ell \left[\pi^{1/2}\exp(\frac{-\kappa_x^2}{4} \times 2v_0\frac{\sin\delta}{\delta})\right]. \tag{2.11}$$

Now expanding the diffrential operator using the identity

$$\frac{\partial^n}{\partial\kappa_x^n}\exp\left(\frac{-\kappa_x^2}{4}\right) = \exp\left(\frac{-\kappa_x^2}{4}\right)\frac{1}{2^n}\left[\exp\left(\frac{\kappa_x^2}{4}\right)\frac{\partial^n}{\partial(\kappa_x/2)^n}\exp\left(\frac{-\kappa_x^2}{4}\right)\right], \tag{2.12}$$

and using the definition of Hermite polynomial of order n in the above equation

$$H_n(x) = (-1)^n e^{x^2}\frac{d^n}{dx^n}e^{-x^2}, \tag{2.13}$$

we can rewrite Equation 2.12 as

$$\frac{\partial^n}{\partial\kappa_x^n}\exp\left(\frac{-\kappa_x^2}{4}\right) = \exp\left(\frac{-\kappa_x^2}{4}\right)\left(-\frac{1}{2}\right)^n H_n(\kappa_x/2). \tag{2.14}$$

Using Equations 2.9-2.14 we can now write the diffracted field for a long and thin slit as

$$U_f(x,y) = C''_\ell\exp\left(-\frac{\kappa_x^2}{4}\right)\sum_{m=0}^{\ell}\frac{\ell!}{m!(\ell-m)!} \times \left(-\frac{1}{2}\right)^m H_m(\kappa_x/2)(iv_0)^{\ell-m}\frac{\partial^{\ell-m}}{\partial\delta^{\ell-m}}\left(\frac{\sin\delta}{\delta}\right), \tag{2.15}$$

where all non-essential factors have been absorbed into C''_ℓ.

Expressing κ_x in terms of β and v_0 from Equations 2.5 and 2.9 we can now write $\kappa_x = \frac{\beta}{v_0}$. We know that the intensity distribution $I_\ell \propto |U_f|^2$. Using the $U_f(x,y)$ found in Equation 2.15, we can write the intensity distributions for the first few ℓ values as follows.

First we note that for $\ell = 0$, we have

$$I_0 = I_{00} \exp(-2\beta^2 w_0^2/d^2) \left(\frac{\sin\delta}{\delta}\right)^2. \tag{2.16}$$

In order to express the other I_ℓ, let us define $F_0 = \exp(-2\beta^2 w_0^2/d^2) \left(\frac{\sin\delta}{\delta}\right)^2$. Then, $I_0 = I_{00} F_0$. For simplicity of writing, let us define f_ℓ as the ℓth order derivatives of $\mathrm{sinc}(\delta)$ with respect to δ. Recalling ν from Equation 2.5, we can express

$$I_1 = I_{10} F_0 \left[(2\nu^2 f_1 \cos\theta)^2 + (\beta - \nu^2 f_1 \sin\theta)^2\right], \tag{2.17}$$

$$\begin{aligned} I_2 = I_{20} F_0 \big[&(\beta^2 - 2\nu^2\cos\theta - 4\beta\nu^2 f_1 \sin\theta - 4\nu^4 f_2 \cos 2\theta)^2 \\ &+ (2\nu^2 \sin\theta - 4\beta\nu^2 f_1 \cos\theta + 4\nu^4 f_2 \sin 2\theta)^2\big], \end{aligned} \tag{2.18}$$

$$\begin{aligned} I_3 = I_{30} F_0 \big[&\big\{(\beta^3 - 6\beta\nu^2\cos\theta) - 6\nu^2 f_1(\beta^2 \sin\theta - 2\nu^2 \sin 2\theta) \\ &-12\beta\nu^4 f_2 \cos 2\theta + 8\nu^6 f_3 \sin 3\theta\big\}^2 \\ &+ \big\{6\beta\nu^2 \sin\theta - 6\nu^2 f_1(\beta^2 \cos\theta - 2\nu^2 \cos 2\theta) \\ &+ \ 12\beta\nu^4 f_2 \sin 2\theta + 8\nu^6 f_3 \cos 3\theta\big\}^2\big], \end{aligned} \tag{2.19}$$

$$\begin{aligned} I_4 = I_{40} F_0 \big[&\big\{\beta^4 - 12\beta^2\nu^2\cos\theta + 12\nu^4\cos 2\theta - 8\nu^2 f_1(\beta^3 \sin\theta - 6\beta\nu^2 \sin 2\theta) \\ &-24\nu^4 f_2(\beta^2 \cos 2\theta - 2\nu^2 \cos 3\theta) + 32\nu^6\beta f_3 \sin 3\theta + 16\nu^8 f_4 \cos 4\theta\big\}^2 \\ &+ \big\{(12\beta^2\nu^2 \sin\theta - 12\nu^4 \sin 2\theta) - 8\nu^2 f_1(\beta^3 \cos\theta - 6\beta\nu^2 \cos 2\theta) \\ &+ \ 24\nu^4 f_2(\beta^2 \sin 2\theta - 2\nu^2 \sin 3\theta) + 32\beta\nu^6 f_3 \cos 3\theta - 16\nu^8 f_4 \sin 4\theta\big\}^2\big]. \end{aligned} \tag{2.20}$$

As done before all non-essential factors have been absorbed into the constants $I_{\ell 0}$. The

functions $f_l(\delta)$ for $\ell = 0 - 4$ are given by

$$
\begin{aligned}
f_0(\delta) &= \frac{\sin\delta}{\delta}, \\
f_1(\delta) &= \frac{1}{f_0}\frac{\partial f_0}{\partial \delta} = \frac{1}{\delta}[\delta\cot\delta - 1], \\
f_2(\delta) &= \frac{1}{f_0}\frac{\partial^2 f_0}{\partial \delta^2} = \frac{1}{\delta^2}[2 - \delta^2 - 2\delta\cot\delta], \\
f_3(\delta) &= \frac{1}{f_0}\frac{\partial^3 f_0}{\partial \delta^3} = \frac{1}{\delta^3}[-6 + 3\delta^2 + \delta(6 - \delta^2)\cot\delta], \\
f_4(\delta) &= \frac{1}{f_0}\frac{\partial^4 f_0}{\partial \delta^4} = \frac{1}{\delta^4}[24 - 12\delta^2 + \delta^4 - 4\delta(6 - \delta^2)\cot\delta].
\end{aligned} \tag{2.21}
$$

The theoretical results in the expressions 2.17-2.20 were computed for a long slit illuminated with LGV beams of orders $\ell = 1 - 4$. Let us define the normalized slit distance as $\zeta = (z - z_0)/z_R$ from the beam waist. Figure 2.3 shows these computed results scaled in terms of the variable β (horizontal) and δ (vertical). For these plots an infinitely long slit of width $d = 50\,\mu$m was used under the illumination of an LGV beam of wavelength $\lambda = 0.6328\,\mu$m, with a waist size $w_0 = 198\,\mu$m. The focal length in the $2f$ arrangement was $f = 10$cm.

In all cases, the incident beam is centered on the slit. When the slit is at the waist of the incident beam ($\zeta = 0$), the incident phase front is planar (no curvature), the diffraction pattern is symmetric about the y axis and has, $\ell + 1$ fringes. As the slit is moved away from the incident beam waist along the beam propagation direction, the diffraction pattern was no longer symmetric about the beam axis and developed a shear relative to the pattern obtained when the slit was at the waist. The shear reached a maximum at $\zeta = 1$ and decreases as ζ increases beyond 1. While the splitting of the diffraction pattern is a direct result of the azimuthal variation of the phase, the shear of the diffraction pattern is a

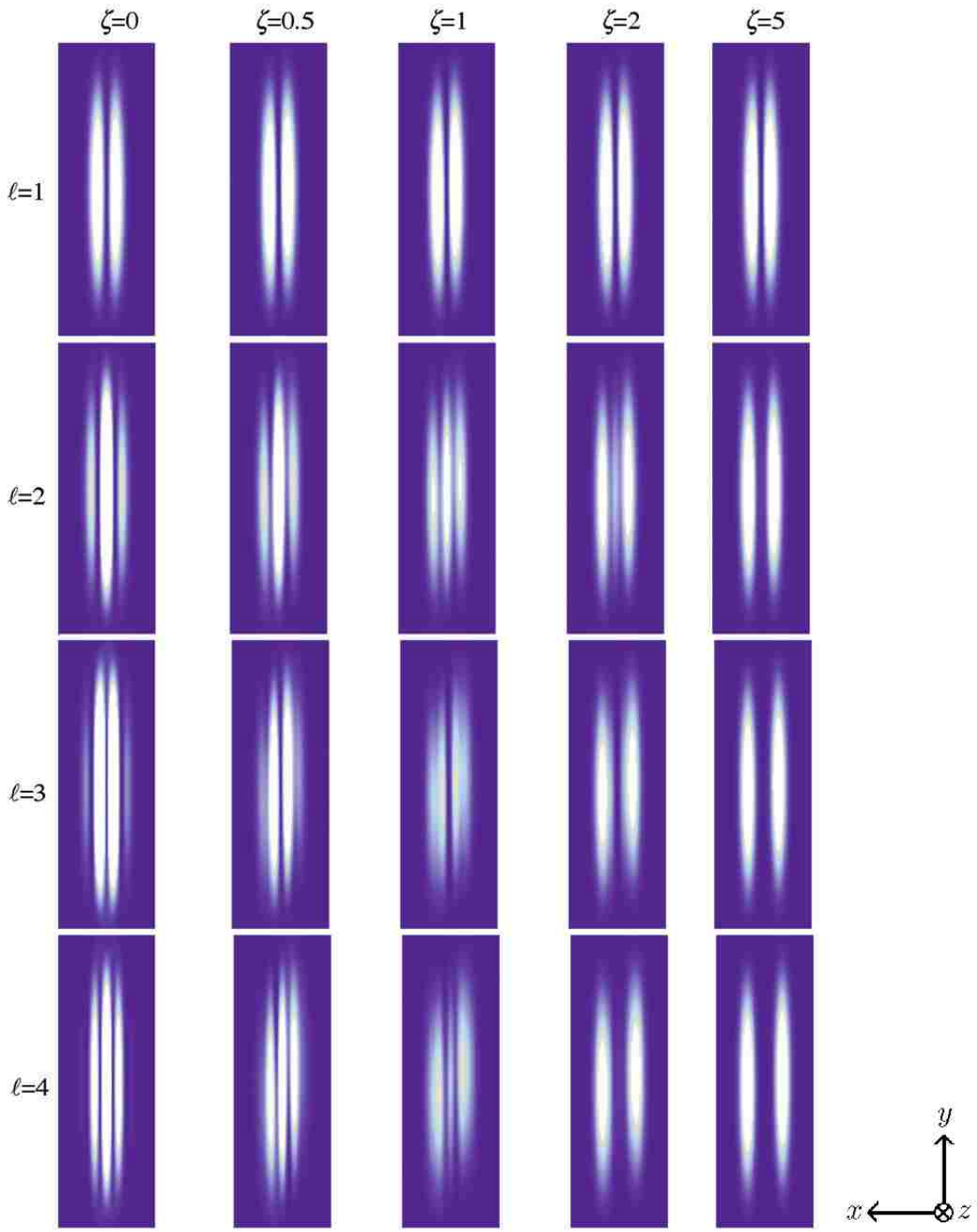

Figure 2.3: Fraunhofer diffraction pattern of a long horizontal slit of width $d = 50\,\mu$m illuminated by LGV beams of wavelength $\lambda = 0.6328\,\mu$m, for different locations of the slit relative to the waist of the incident beam, which made a waist size $w_0 = 198\,\mu$m. This is a greyscale image with white representing brightness.

consequence of the quadratic radial phase variation across the slit, the effect of which depends on the incident phase front curvature which varies with the propagation away from the waist.

The shear of the diffraction pattern is accompanied by another qualitative change, which become more significant for higher values of ℓ. The diffraction pattern for all $\ell \neq 0$ shows two dominant fringes located at $\beta \approx \pm(|\ell| d^2/2w_0^2)^{1/2}$ and $\delta \approx 0$. For example the diffraction pattern for an odd order beam, say $\ell = 3$ beam at the waist has a dark center and four off-center fringes symmetrically about the center (Figure 2.3). At the waist the two inner fringes are brighter than the two outer fringes but as ζ increases, the inner fringes gradually fade out leaving a diffraction pattern dominated by the two outer fringes far from the waist. For an even order say $\ell = 4$ there are five peaks when at the waist, the central fringe is the brightest but as ζ increases the central and the two outer fringes gradually fade away, once again leaving a diffraction pattern with two prominent fringes. An experiment to observe these novel features in the Fraunhofer diffraction of LGV beams was carried out and is described in the next section.

2.3 Experiment

Figure 2.4 shows a side view of the experimental setup. The generation of LGV beams was described in chapter 1. The LGV beam emerging from the mode converter was focused by a 40 cm focal length lens, L_1 to form a waist with an approximate spot size of 198 μm. A slit was placed along the beam propagation direction, such that the LGV beam was normally incident on the slit. The slit was always centered on the beam and long enough to capture the entire beam along its length. Light diffracted by the slit was collected by a lens

L_2 placed one focal length behind the slit, such that the slit was in its front focal plane. The CCD used to record the patterns was located one focal length behind the lens, so as to be in the back focal plane of the lens. Thus the slit, the lens L_2, and the CCD were in the $2f$-geometry. The diffraction pattern recorded by the CCD is the Fourier transform of the incident field limited by the aperture or the Fraunhofer diffraction pattern [25], and is given by Equation 2.1. As the slit location relative to the incident LGV beam waist was varied, the configuration of the slit, lens L_2 and the CCD remained in $2f$-geometry. These three objects were always moved as a single unit, with no relative change of distance between them. Thus the pattern recorded by the CCD was always the Fourier transform of the slit illuminated by the incident LGV beam.

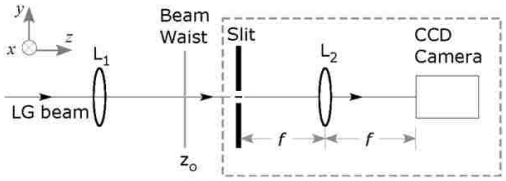

Figure 2.4: A side view of the experimental set-up. Lens L_1 forms a waist of the incident beam at $z = z_0$. The slit, lens L_2 and the CCD camera are in $2f$-geometry. The apparatus enclosed by the dashed box is translated along the beam axis near the waist, with no relative change in distance of the constituents.

2.4 Results and Conclusions

The diffraction patterns when a horizontal slit is placed at the waist $z - z_0 = 0$ is shown in Figure 2.5. The patterns in the left column are the CCD images. A quantitative comparison of the experimental and theoretical results is shown in the panels to the right of the experimentally recorded profiles. The dots represent the experimental intensity values extracted by scanning a CCD image through its center. To locate the image center,

experimentally recorded image profiles were exported to Mathematica. A spline smoothing transformation was applied to the image data before locating the image center using FindMaximum and FindMinimum with an approximate starting point, to search for local maxima (bright center) or minima (dark center). The diffraction of the fundamental beam ($\ell = 0$) when the slit is located at the beam waist, was used to find a scale factor to convert pixel size into actual length. It was found that 180 pixels $\approx$ 1 mm. Super-imposed on these experimentally extracted data, are the theoretical curves computed from Equations 2.17-2.20 which were found indistinguishable from those computed from Equations 2.4. For theoretical calculations, we used $w_0 = 198\mu$m, $\lambda = 633$ nm, $f = 10.0$ cm, slit width was $d = 50\mu$m and length 3 mm, which was large compared to beam waist. To compare theoretical and experimentally recorded intensity profiles, we scaled the theoretical intensity at one maximum to match the corresponding experimental intensity. No other fitting parameters were used.

The incident phase front has no radial phase variation in the plane of the slit at the waist. For $\ell = 0$ we see the familiar sinc square intensity pattern with a maximum at the center. For $\ell = 1$ the diffraction pattern splits into two intensity maxima with a minimum (zero) at the center. For $\ell = 2$ the pattern has three peaks with a maximum at the center. In general for LGV beam of topological charge ℓ, the diffraction pattern consists of $\ell + 1$ maxima, which are located symmetrically about the beam axis. For odd ℓ, there is a null (zero) at the center and for even ℓ there is a maximum at the center. These results at the waist agree with those reported in [17]. It can be seen that in all cases experimental data follow the theoretical curves well.

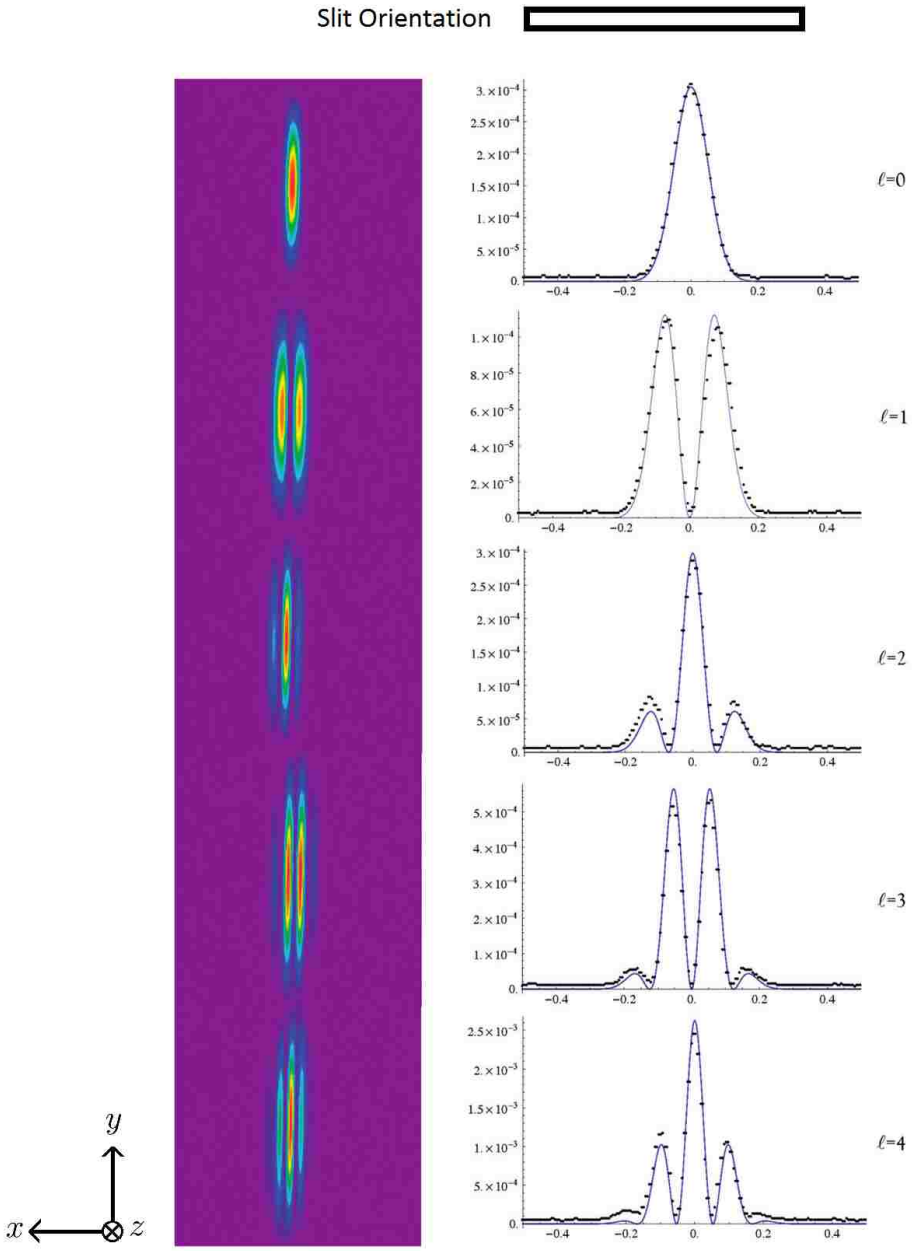

Figure 2.5: A comparision of the experimentally recorded diffraction pattern (dots) with the theoretical predictions (continuous line) for a slit at the incident beam waist $z - z_0 = 0$. The horizontal axis in the graph is the distance from the center in mm, and the vertical axis in the graph represents relative intensity.

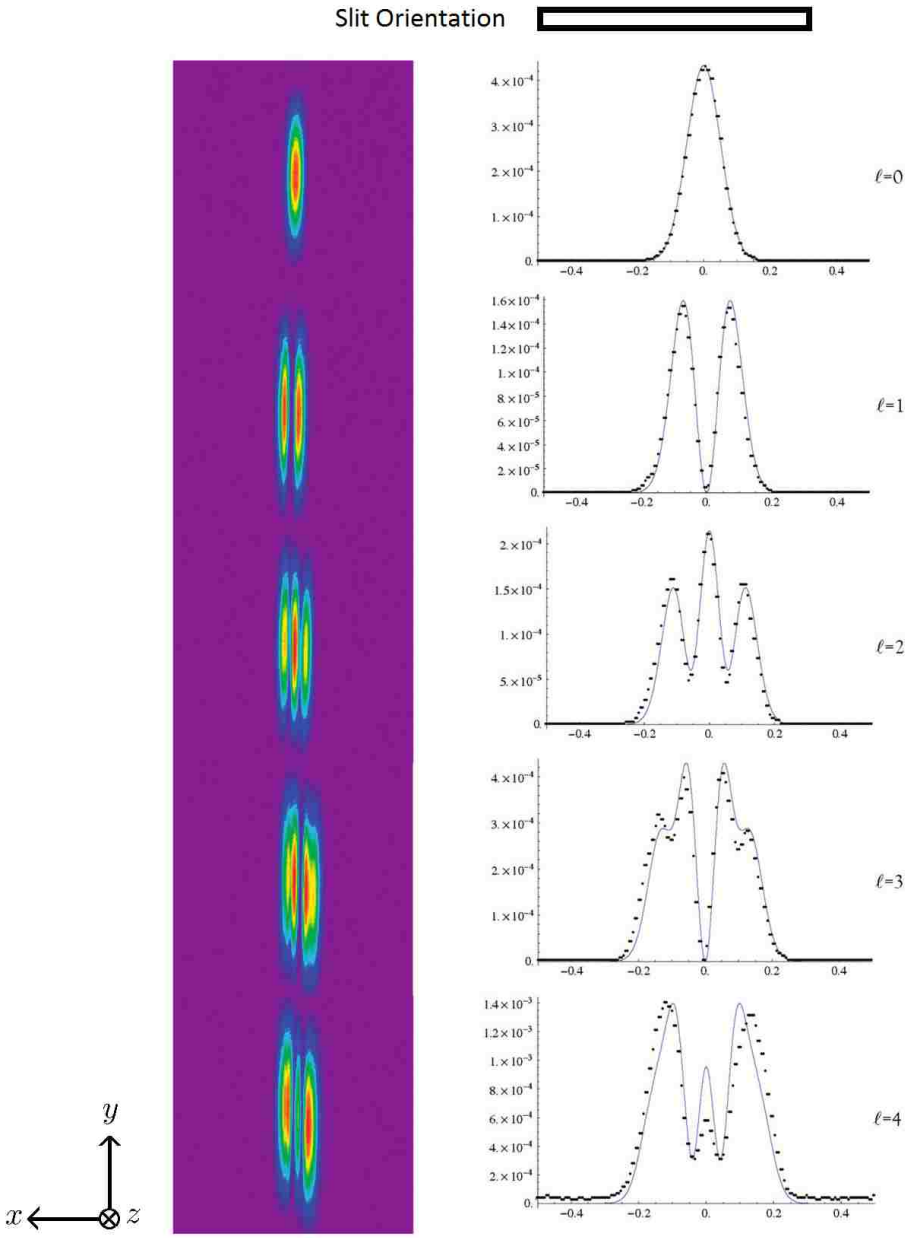

Figure 2.6: A comparision of the experimentally recorded diffraction pattern (dots) with the theoretical predictions (continuous line) for a slit at $\zeta = (z - z_0)/z_R = -1$. The horizontal axis in the graph is the distance from the center in mm, and the vertical axis in the graph represents relative intensity.

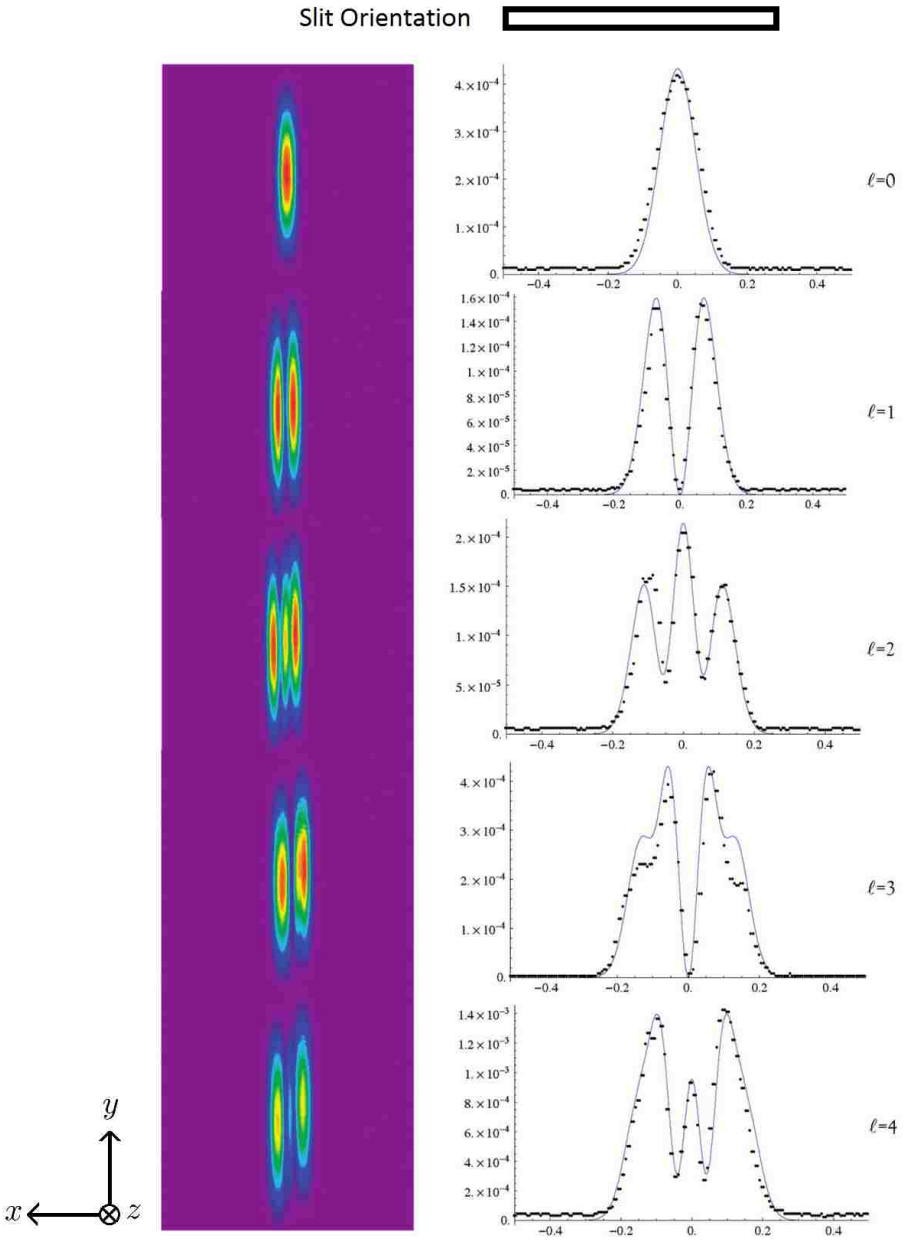

Figure 2.7: A comparision of the experimentally recorded diffraction pattern (dots) with the theoretical predictions (continuous line) for a slit at $\zeta = (z - z_0)/z_R = 1$. The horizontal axis in the graph is the distance from the center in mm, and the vertical axis in the graph represents relative intensity.

The effect of quadratic variation of phase with radial distance from the center or, equivalently, phase front curvature, was explored by placing the slit at different locations before and after the waist of the incident LGV beam. As the beam is propagating in the

$+z$-direction, phase front curvature $R(z)$ is positive (diverging beam) for $\zeta > 0$ and negative (converging beam) for $\zeta < 0$.

Figure 2.6 shows the diffraction patterns when the slit is placed one Rayleigh range before the waist ($\zeta = -1$) so that the beam incident on the slit is a converging beam. It was found that the diffraction pattern was sheared. Figure 2.7 shows the diffraction patterns when the slit is placed one Rayleigh range after the waist ($\zeta = 1$) such that the incident beam is a diverging beam. In this case the shear is opposite to that seen in Figure 2.6. Thus the direction of shear depends on the sign of curvature $R(z)$, i.e. whether the beam is converging or diverging.

The shear of the diffraction pattern was quantified in terms of the angle (positive in the counterclockwise sense) that a line from the center of the diffraction pattern to the dominant off-center diffraction peak makes with the horizontal.

Variation of this angle with ζ is shown in Figure 2.8, where the dots represent the experimental values and the continuous curve is derived from Equations 2.17-2.20. For slit positions before the waist ($\zeta < 0$), where the beam has a converging phase front (negative curvature), the angle of shear is negative for positive values of ℓ, and positive for negative values of ℓ. As the waist is approached, the angle of shear decreases in magnitude to zero at the waist. For slit positions after the waist ($\zeta > 0$), where the beam has a diverging phase front (positive curvature), the angle of shear becomes positive for positive values of ℓ, and negative for negative values of ℓ. For all values of ℓ, the maximum magnitude of shear is attained near $\zeta \approx \pm 1$, where the curvature has its maximum value. The shear varies rapidly in the waist region where it depends on ℓ and the sign of ℓ as well. At beam waist and far from it ($\zeta \gg 1$), the radius of curvature is zero and small respectively, thus

the shear becomes negligible.

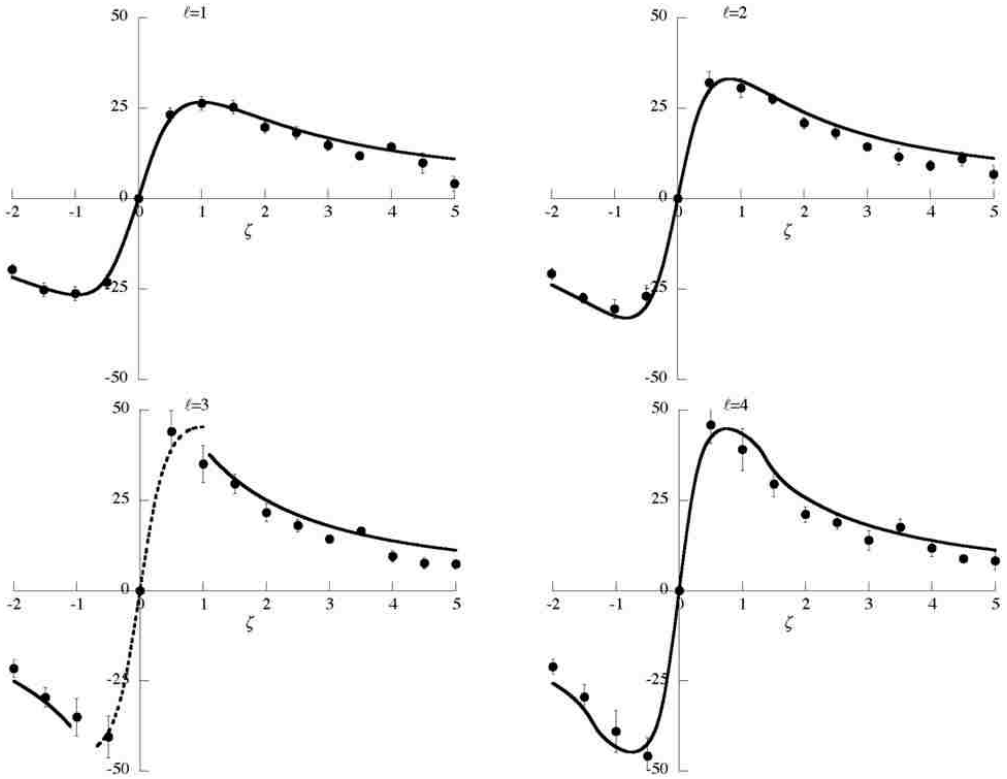

Figure 2.8: Variation of the angle of shear (in degrees along the vertical axes) as a function of the normalized slit displacement $\zeta = (z - z_0)/z_R$ from the waist.

On investigating the regions away from the waist we find that, as we move away from the waist region $|\zeta| > 0$, the phase front curvature changes, thus causing a change in the diffraction patterns as well. It is observed that the relative peak intensities change. For example, for $\ell = 3$, the dominant diffraction peaks start out to be the two inner peaks when the slit is at the waist. As $|\zeta|$ increases, the intensity of the dominant inner peaks decreases until $|\zeta| = 1$, beyond which the outer peaks become the dominant as seen in Figure 2.3. For $|\zeta| > 1$, the inner peaks essentially fade away.

The dashed curve in Figure 2.8 for $\ell = 3$ shows the angle of shear for the inner peaks when they are the dominant peaks and the solid curve shows the angle of shear for the

outer peaks when they are the dominant peaks. The shear of the diffraction pattern changes slightly with distance from the center of the pattern. The sense of shear changes with the sign of ℓ. We can summarize this behavior by saying that as the slit position varies from $(-1 \leq \zeta \leq 1)$, the diffraction pattern shears in a counter-clockwise sense for positive values of ℓ and in a clockwise sense for negative values of ℓ. As the slit position is beyond the rayleigh range, that is $|\zeta| > 1$ the amount of shear reduces, but the sense of shear remains the same, this is seen in Figure 2.8.

As the slit is moved farther away from the waist ($\zeta \gg 1$), the diffraction pattern evolves into a pattern dominated by two peaks irrespective of ℓ. The peaks are located equidistant from the center and their location depends on the topological charge ℓ through $\beta \approx \pm(|\ell|d^2/2w_0^2)^{1/2}$ and $\delta \approx 0$. The effect of topological charge is revealed in ℓ-dependent positions of the peak. For odd values of ℓ there is null at the center while for even values there is a weak maximum at the center but with intensity much weaker than the dominant off-center peaks. Thus in Figure 2.9 this peak is invisible. It is important to note that if the quadratic phase variation is neglected, the diffraction pattern reverts to being similar to that seen when the slit is located in the waist region.

In conclusion, the effect of the quadratic radial variation of phase (phase front curvature) on the far field diffraction of Laguerre Gauss vortex beams by a thin slit have been studied. It is found that without the quadratic radial phase variation (planar phase front), the central diffraction maximum consists of $\ell + 1$ fringes, which are symmetrically located about the center of the pattern. When the incident phase front radius of curvature $R(z)$ is nonzero, the diffraction pattern is sheared relative to the pattern produced by a planar phase front. The angle of shear depends on the sign of the radius of curvature $R(z)$

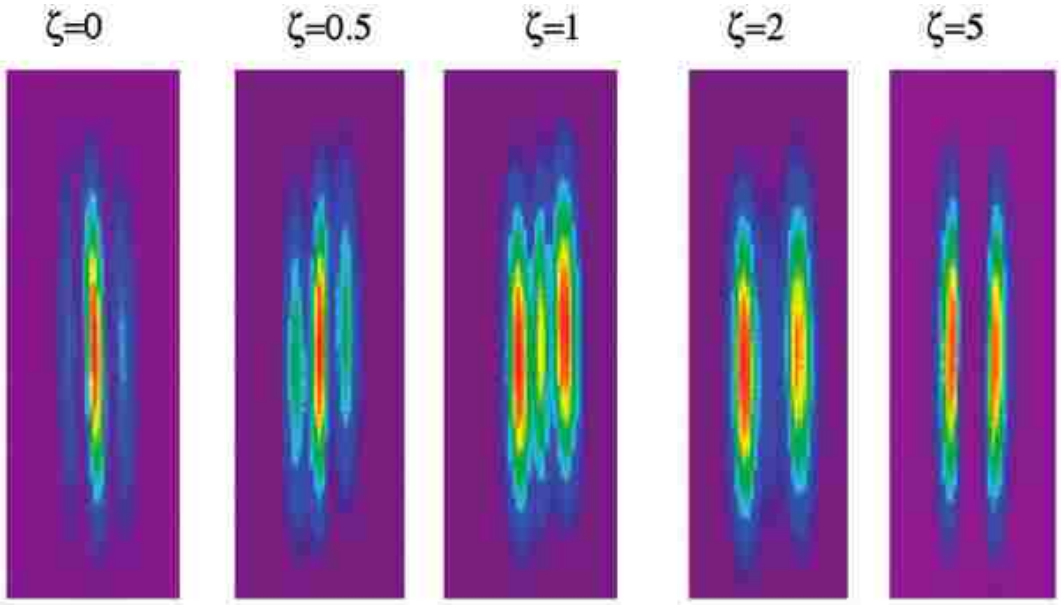

Figure 2.9: Evolution of the diffraction pattern from a three-peak pattern (corresponding to $\ell = 2$) for the slit at the waist ($\zeta = 0$), to a two dominant peak pattern for the slit far from the waist ($\zeta = 5$).

and the sign of the topological charge ℓ. The radius of curvature depends on the position of the slit. The same diffraction pattern can be obtained for two different combinations of signs of ℓ and $R(z)$. For example, the diffraction pattern for $+\ell$ at $z = +z_R$ and $-\ell$ at $z = -z_R$ are the same. Thus knowing the waist position is important in determining the magnitude and sign of the topological charge by studying the Fraunhofer diffraction pattern of the beam. The number of fringe N in the diffraction pattern gives $|\ell| = N - 1$, the amount of shear gives the Radius of curvature $R(z)$, and the sense of shear gives the sign of ℓ.

For slit positions far from the waist, the diffraction pattern evolves into a symmetric pattern with two dominant fringes for all LGV beams independent of ℓ. Experimental results are in good agreement with the theoretical predictions. It is clear that in order to understand the diffraction of LGV beams we must take into account, not only their

azimuthal phase variation but also the quadratic radial phase variation due to the curvature of the phase front.

Chapter 3

Circular Aperture Diffraction

3.1 Introduction

Diffraction of the Laguerre Gaussian vortex (LGV) beams by a thin slit exhibits many unexpected features which lead to diffraction patterns that are very different form the sinc-squared pattern as seen in chapter 2. Most optical instruments however, have circular apertures. These apertures are usually aligned such that the aperture axis coincides with the incoming beam axis. One everyday example of devices that have apertures and have to be so aligned is a camera. But there are some applications where the aperture, grating or mirror is deliberately misaligned to capture a portion of the beam that may not be along the beam axis. For example, in Multiple-Mirror Telescopes (MMT) the misalignment of mirrors and apertures is used for aberration sensing and high resolution image reconstruction [31].

When a circular aperture is illuminated by the LGV beams carrying orbital angular momentum, the diffraction patterns can be described in terms of Bessel functions of order that depends on the angular momentum index of the incident LGV beam, and the ratio of the aperture size to the beam spot size. The diffraction of Laguerre-Gauss vortex (LGV) beams by a circular aperture, when the beam axis coincides with the aperture axis shows many unexpected new features. When the beam axis does not coincide with the aperture axis, many of these features begin to dissipate.

In this chapter an analytical description of the diffraction of LGV beams at a circular aperture is presented, which are compared to the experimentally recorded diffraction

patterns. The effects of phase front curvature on the diffraction pattern are studied. The far field diffraction of LGV beams incident on a laterally misaligned circular aperture is investigated. Evolution of the diffraction pattern and the vortex structure are studied for various beam axis displacements relative to the aperture axis.

Consider a field $U_{in}(x', y', z)$ propagating in the $+z$ direction illuminating a two-dimensional aperture A in the $x' - y'$ plane. The diffracted field in the far zone, the Fraunhofer diffraction, is proportional to the Fourier transform of the incident field distribution in the plane of the aperture. By using the $2f$-geometry, explained in chapter 1, we observe the Fraunhofer diffraction by an aperture [25]. The diffracted field in the back focal plane of the lens is given by

$$U_f(x, y) = \frac{ik}{2\pi f} \iint_A dA U_{in}(x', y', z) \times \exp\left[-\frac{ik}{f}(xx' + yy')\right], \tag{3.1}$$

where $k = 2\pi/\lambda$ is the wavenumber, λ is the wavelength of light, z is the location of the aperture measured from the position of the beam waist, and x, y are the transverse coordinates of a point in the back focal plane of the lens, the observation plane.

If U_{in} is a plane wave incident on a circular aperture the resultant diffracted field intenstity results in the Airy pattern [32] given by

$$I(\theta) = I_0 \left(\frac{2J_1(ka\sin\theta)}{ka\sin\theta}\right)^2, \tag{3.2}$$

where I_0 is the maximum intensity at the center of the diffraction pattern, J_1 is the Bessel function of the first kind of order one, θ is the angle of observation, $k = 2\pi/\lambda$, and a is the radius of the aperture.

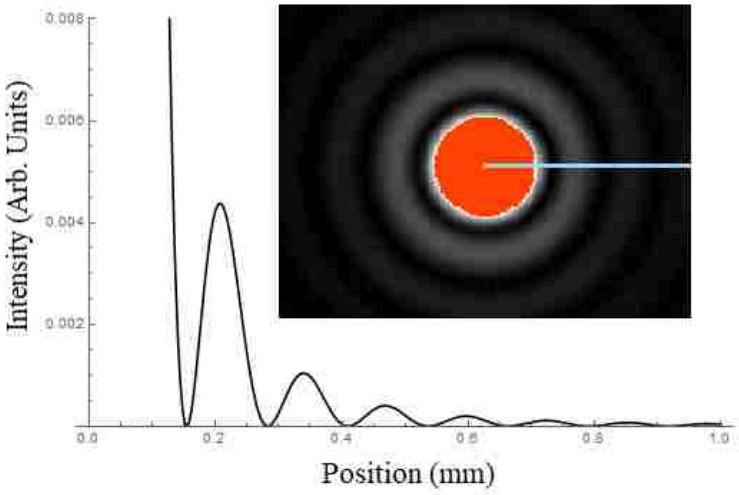

Figure 3.1: Diffraction of a plane wave by a circular aperture results in the airy pattern. The inlaid image is the experimentally recorded pattern, the central portion is overexposed to bring out the details in the outer rings, the graph is the theoretically predicted intensity from the center of the diffraction pattern to the outer edge following the line.

3.2 Theory

For an incident Laguerre-Gauss Vortex (LGV) beam (radial index, $p = 0$) the incident field can be written in the cylindrical coordinates as

$$U_{in}(\rho', \phi', z) = \text{const} \times \left(\frac{\sqrt{2}\rho'}{w(z)} e^{i\phi} \right)^{\ell} \times \exp\left[-\frac{\rho'^2}{w(z)w_0} \left(1 - i\frac{z}{z_R} \right) + ikz - i(\ell+1)\theta(z) \right], \tag{3.3}$$

where $\rho' = \sqrt{x'^2 + y'^2}$ is the distance from the beam axis, $z_R = \pi w_0^2/\lambda$ the Rayleigh range, $w(z) \equiv w_0\sqrt{1 + z^2/z_R^2}$ has a minimum value of w_0 at the waist. The waist is at $z = 0$, the position of the aperture is z, and $\theta(z) = \tan^{-1}(z/z_R)$ is the Guoy's phase of the beam. The primed coordinates are for the aperture plane, and the non-primed coordiantes are for the observation plane. In this expression, L_p^{ℓ} is the associated Laguerre polynomial, when $p = 0$, $L_0^{\ell}(x) = 1$, for each ℓ.

3.2.1 Centered Beam

Let us look at the case of a beam centered on the aperture. Equation 3.1 gives the diffracted field. Cylindrical coordinates with z as the direction of propogation is the natural coordinate system to use with an LGV beam. The expression $(xx' + yy')$ in these coordinates becomes $\rho\rho' \cos\phi \cos\phi' + \rho\rho' \sin\phi \sin\phi'$.

For a circular aperture of radius a, the diffracted field can be written as,

$$U_f(\rho, \phi, z) = \text{const} \int_0^a \int_0^{2\pi} \rho' d\rho' d\phi' U_{in}(\rho', \phi', z) \times \exp\left[\frac{-ik}{f}(\rho\rho' \cos\phi \cos\phi' + \rho\rho' \sin\phi \sin\phi')\right]. \tag{3.4}$$

Here the term $\exp[ikz - i(\ell + 1)\theta(z)]$ has been absorbed into the constant. Using a substitution of $s = \sqrt{2}\rho'/w$ and realizing that $cos(\phi - \phi') = \cos\phi \cos\phi' + \sin\phi \sin\phi'$, the diffracted field in the observation plane can be written as

$$U_f(\rho, \phi, z) = \text{const} \times 2\pi e^{i\ell\phi} \int_0^{\sqrt{2}a/w} ds s^{\ell+1} e^{-\frac{s^2}{2}\left(1 - i\frac{z}{z_R}\right)} \times \frac{1}{2\pi} \int_0^{2\pi} d\phi' \exp\left[-i\ell(\phi - \phi') - \frac{ikw}{\sqrt{2}f}\rho s \cos(\phi - \phi')\right]. \tag{3.5}$$

Using two properties of Bessel functions we can evaluate the integral over ϕ'.

$$J_n(x) = \frac{1}{2\pi i^n} \int_0^{2\pi} e^{ix\cos\phi'} e^{in\phi'} d\phi' \quad \text{and} \quad J_{-m}(x) = (-1)^m J_m(x). \tag{3.6}$$

Thus, the integral over ϕ' is $J_\ell(kw\rho s/\sqrt{2}f)$, the ℓth order Bessel function of the first kind. Changing the variables of the resulting integral by introducing $u = sw/\sqrt{2}a$, so that the

integral now is from $u = 0$ to $u = 1$ we can rewrite the diffracted field as,

$$U_f(\rho,\phi) = \text{const} \times 2\pi \left(\frac{\sqrt{2}a}{w}\right)^{\ell+1} e^{i\ell\phi}(-i)^{\ell} \int_0^1 duu^{\ell+1} e^{-\frac{a^2u^2}{w^2}\left(1-i\frac{z}{z_R}\right)} J_\ell\left(\frac{k\rho au}{f}\right). \quad (3.7)$$

In general, Equation 3.7 must be evaluated numerically. For a special case where $\theta(z = 0) = 0$, which corresponds to incident beam waist at the aperture, the integral can be evaluated as an infinite series of Bessel functions [30]. On the otherhand, if the spot size w is large compared to the aperture size a, then the u^2 term in the exponent is small over the aperture. Thus for a postition far from the input waist, we may ignore the quadratic variation of the incident phase as well as the gaussian envelope over the aperture. This simplifies the above equation to

$$\begin{aligned} U_f(\rho,\phi) &\approx \text{const} \times \int_0^1 duu^{\ell+1} \text{exp}\left[-\frac{a^2}{w(0)w_0}e^{-i\theta(0)}\right] J_\ell\left(\frac{k\rho au}{f}\right), \\ &= \text{const} \times \exp\left[-\frac{a^2}{w(0)w_0}e^{-i\theta(0)}\right] \left[\frac{J_{\ell+1}\left(\frac{ka\rho}{f}\right)}{\left(\frac{ka\rho}{f}\right)}\right]. \end{aligned} \quad (3.8)$$

Small argument expansion of the Bessel function is

$$\begin{aligned} J_\ell(z) &= \left(\frac{z}{2}\right)^{\ell} \sum_{m=0}^{\infty} \frac{(-1)^m}{m!(\ell+m)!}\left(\frac{z}{2}\right)^{2m}, \\ &= \frac{1}{\ell!}\left(\frac{z}{2}\right)^{\ell} - \frac{1}{(\ell+1)!}\left(\frac{z}{2}\right)^{\ell+2}. \end{aligned} \quad (3.9)$$

Using Equation 3.9 we obtain

$$\frac{J_{\ell+1}\left(\frac{ka\rho}{f}\right)}{\left(\frac{ka\rho}{f}\right)} \approx \frac{1}{2^{\ell+1}(\ell+1)!}\left(\frac{ka\rho}{f}\right)^{\ell}. \quad (3.10)$$

It may be seen that, as $\rho \to 0$, $U_f \to 0$. Hence the center of the diffraction pattern is always dark for all $\ell \neq 0$.

3.2.2 Misaligned Aperture

To study the effects of lateral misalignment we first look at a beam that has its axis of propagation parallel to the axis of the aperture, but is separated by a distance ρ_0 as shown in the Figure 3.2. Using the ratio ρ_0/a we can compare the distance of separation of the axes to the radius of the beam, where $\rho_0/a = 0$ implies that both the axes coincide, and $\rho_0/a = 1$ implies that both the axes are a radius a away from each other.

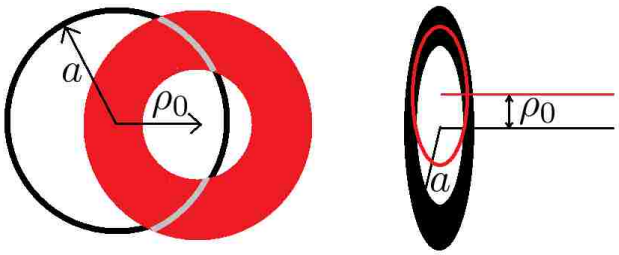

Figure 3.2: The aperture is the black circle and the beam is the red circle. The left most image shows, the aperture and the beam, when viewed along the propagation direction. The center image shows how the beam axis and the aperture axis are separated by ρ_0.

Equation 3.1 gives the diffracted field. When diffracted by a circular aperture, the diffraction integral can be rewritten as

$$U_f^\ell = \frac{ik}{2\pi f}\int_0^a \rho' d\rho' \int_0^{2\pi} U_{in}^\ell e^{-ik\rho\rho' cos(\phi-\phi')/f} d\phi'. \tag{3.11}$$

For an LGV beam in the waist plane and the incident light centered at (x_0, y_0), and $s = \text{sign}(\ell)$ the field is given by

$$U_{in}^\ell(x,y) = C_\ell \left[\frac{(x'-x_0)}{w} + is\frac{(y'-y_0)}{w}\right]^{|\ell|} \times e^{-\left[(x'-x_0)^2+(y'-y_0)^2\right]/w^2}. \tag{3.12}$$

In Cylindrical coordinates the incident light is centered at (ρ_0, ϕ_0). Here ρ_0 is the distance between the aperture axis and the axis of propagation of the incident beam. The field in

cylindrical coordinates is given by

$$U_{in}^{\ell}(\rho,\phi) = C_l \sum_{r=0}^{|\ell|} \frac{|\ell|!}{r!(|\ell|-r)!} \left(\frac{-\rho_0}{w} e^{is\phi_0}\right)^{|\ell|-r} \left(\frac{\rho'}{w} e^{is\phi'}\right)^{r} \times e^{-[\rho'^2+\rho_0^2-2\rho'\rho_0\cos(\phi'-\phi_0)]/w^2}. \tag{3.13}$$

The diffraction integral now becomes

$$U_{f}^{\ell}(\rho,\phi) = \frac{ik}{2\pi f} \int_0^a \rho' d\rho' \int_0^{2\pi} C_\ell \sum_{r=0}^{|\ell|} \frac{|\ell|!}{r!(|\ell|-r)!} \left(\frac{-\rho_0}{w} e^{is\phi_0}\right)^{|\ell|-r} \left(\frac{\rho'}{w} e^{is\phi'}\right)^{r} \times e^{-[\rho'^2+\rho_0^2-2\rho'\rho_0\cos(\phi'-\phi_0)]/w^2} \times e^{-ik\rho\rho'\cos(\phi-\phi')/f} d\phi'. \tag{3.14}$$

We simplify the above integral by changing the order of the integral and the summation, and taking all the quantities that do not depend on the variables of integration out of the integral. It leads to

$$U_{f}^{\ell}(\rho,\phi) = \frac{ik}{2\pi f} C_\ell e^{-\left(\frac{\rho_0}{w}\right)^2} \sum_{r=0}^{|\ell|} \frac{|\ell|!}{r!(|\ell|-r)!} \left(\frac{-\rho_0}{w} e^{is\phi_0}\right)^{|\ell|-r} \int_0^a \rho' d\rho' \left(\frac{\rho'}{w}\right)^{r} e^{-\left(\frac{\rho'}{w}\right)^2} \times \int_0^{2\pi} d\phi' e^{irs\phi'} \times e^{\frac{2\rho'\rho_0}{w^2}\cos(\phi'-\phi_0)} \times e^{-i\frac{k\rho\rho'}{f}\cos(\phi-\phi')}. \tag{3.15}$$

Let us work on the ϕ' integral in more detail. Multiplying and deviding the entire exponent with a, the ϕ' integral now has the form

$$\int_0^{2\pi} d\phi' \times \exp\left[irs\phi' - \frac{i\rho'}{a}\left(\frac{ka\rho}{f}\cos(\phi-\phi') + \frac{2ia^2\rho_0}{w^2 a}\cos(\phi'-\phi_0)\right)\right]. \tag{3.16}$$

Using $\cos(A-B) = \cos A\cos B + \sin A \sin B$ we can write the exponent as

$$irs\phi' - \frac{i\rho'}{a}\left[\cos\phi'\left(\frac{ka\rho}{f}\cos\phi + \frac{2ia^2\rho_0}{w^2 a}\cos\phi_0\right) + \sin\phi'\left(\frac{ka\rho}{f}\sin\phi + \frac{2ia^2\rho_0}{w^2 a}\sin\phi_0\right)\right]. \tag{3.17}$$

Define,

$$\xi \cos\gamma = \frac{ka\rho}{f}\cos\phi + \frac{2ia^2\rho_0}{w^2 a}\cos\phi_0,$$
$$\xi \sin\gamma = \frac{ka\rho}{f}\sin\phi + \frac{2ia^2\rho_0}{w^2 a}\sin\phi_0. \tag{3.18}$$

Then we have,

$$\xi e^{i\gamma} = \xi\cos\gamma + i\xi\sin\gamma, \text{and}$$
$$\xi e^{i\gamma} = \frac{ka\rho}{f}e^{i\phi} + \frac{2ia^2\rho_0}{w^2 a}e^{i\phi_0}. \tag{3.19}$$

Let us also define $A = \frac{ka\rho}{f}$, $B = \frac{2\rho_0 a}{w^2}$, where the maximum value of ρ' is a, and $\varepsilon = \phi_0 - \phi$.

Equation 3.19 can be rewritten as

$$\begin{aligned}\xi e^{i\gamma} &= Ae^{i\phi} + iBe^{i(\phi+\varepsilon)} \\ &= e^{i\phi}\left(A + iBe^{i\varepsilon}\right) \\ &= e^{i\phi}(A + i(B\cos\varepsilon + iB\sin\varepsilon)) \\ &= e^{i\phi}(A - B\sin\varepsilon + iB\cos\varepsilon).\end{aligned} \tag{3.20}$$

Thus $\xi = (A - B\sin\varepsilon + iB\cos\varepsilon)$, and $\gamma = \phi$. The diffraction integral can now be rewritten as

$$U_f^\ell(\rho,\phi) = \frac{ikC_l}{2\pi f}e^{-\rho_0^2/w^2}\sum_{r=0}^{|\ell|}\frac{|\ell|!}{r!(|\ell|-r)!}\left(\frac{-\rho_0}{w}e^{is\phi_0}\right)^{|\ell|-r}u_r \tag{3.21}$$

where,

$$u_r = \int_0^a \rho' d\rho'\left(\frac{\rho'}{w}\right)^r e^{-\rho' 2/w^2}\int_0^{2\pi} d\phi' e^{irs\phi' - i\frac{\rho'}{a}\xi\cos(\phi'-\gamma)}. \tag{3.22}$$

Using the substitution $\theta = \phi' - \gamma$, the ϕ' integral becomes

$$e^{irs\gamma} \int_{-\gamma}^{2\pi-\gamma} d\theta e^{irs\theta} e^{\frac{-i\rho'\xi}{a}\cos\theta}. \tag{3.23}$$

This integral can be evaluated using the following properties of Bessel functions:

$$J_n(x) = \frac{1}{2\pi i^n} \int_0^{2\pi} e^{ix\cos\phi'} e^{in\phi'} d\phi' \quad \text{and} \quad J_{-m}(x) = (-1)^m J_m(x). \tag{3.24}$$

Equation 3.22 gives

$$u_r = \int_0^a \rho' d\rho' \left(\frac{\rho'}{w}\right)^r e^{-\rho' 2/w^2} \left[2\pi e^{i(\gamma s + \frac{\pi s}{2})r} J_r\left(\frac{\rho'\xi}{a}\right)\right]. \tag{3.25}$$

Now the ρ' integral can be solved by doing the substitution $q = \frac{\rho'\xi}{a}$, which gives $d\rho' = \frac{a}{\xi} dq$ and integrating by parts.

Thus the solution for off-axis illumination is obtained as

$$\begin{aligned} U_f^\ell(\rho,\phi) = \frac{ika^2 C_l}{2\pi f} e^{\frac{-(\rho_0^2+a^2)}{w^2}} \sum_{r=0}^{|\ell|} \frac{|\ell|!}{r!(|\ell|-r)!} \left(\frac{-\rho_0}{w} e^{is\phi_0}\right)^{|\ell|-r} \left(\frac{a}{w}\xi e^{i\gamma} e^{\frac{-i\pi s}{2}}\right)^r \\ \times \left[\frac{J_{r+1}(\xi)}{\xi^{r+1}} + \frac{2a^2}{w^2}\frac{J_{r+2}(\xi)}{\xi^{r+2}} + \left(\frac{2a^2}{w^2}\right)^2 \frac{J_{r+3}(\xi)}{\xi^{r+3}} + \cdots\right]. \end{aligned} \tag{3.26}$$

3.3 Experiment

The method used to produce the Laguerre-Gauss (LG) modes is the same as in chapter 2. Here is a brief description of the procedure. A He:Ne laser equipped with two intra cavity orthogonal fibers intersecting the beam axis, produced Hermite-Gauss (HG) beams. The translation of these fibers can produce some low order HG modes. These HG modes were transformed into LG modes by using an astigmatic mode converter [14]. The detailed description of the experimental set up to generate Laguerre-Gauss Vortex (LGV) beams is

discussed in Chapter 1 Section 1.2.

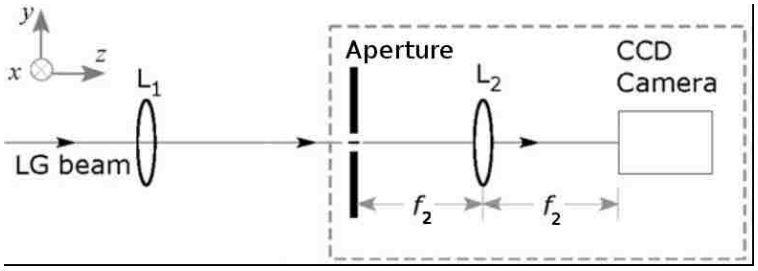

Figure 3.3: A side view of the experimental setup. The LG beam was focused with lens L_1 at the aperture, which lies in the front focal plane of lens L_2, the image plane of the CCD camera lies in the back focal plane. The apparatus in the dashed box is rigidly translated along the beam axis to the desired location.

The LGV beam from the mode converter is focused using a lens L_1 to obtain a desired beam spot size w at the waist. The diffracted light is collected by lens L_2 placed one focal length f_2 behind the aperture and was recorded by a CCD camera located one focal length behind the lens. As the aperture is located in the front focal plane of the lens and the CCD camera is placed in the back focal plane, the image captured by the camera is the Fourier transform of the incident field, this is called the $2f$-geometry.

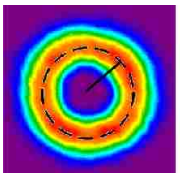

$$w = \sqrt{\ell + 1} w_0$$

Figure 3.4: The radius w of the LGV beam of order ℓ.

At the waist of the LGV beam a circular aperture a of 500μm was placed, such that the LGV beams were normaly incident on the aperture. The aperture was centered on the beam. In order to study how the diffraction pattern varied as aperture size a changed with respect to beam waist size w, an ability to have control of the ratio a/w was required. The focal length of lens L_1 and its position were chosen to obtain various waist sizes. This gave

us a control over the ratio a/w. The exact method used to find the waist size is described in Chapter 1. Using different waist sizes for the same diffracting aperture, a decade of a/w ratios from 0.2 to 2, was obtained. For each ℓ the LGV beam size was taken to be $\sqrt{\ell+1}w_0$ [33]. It was found that 180 pixels $\approx$ 1 mm.

To study the effect of missalignment, the waist size was kept the same as the aperture size, that is $a/w = 1$. We first look at a beam that has its axis of propagation parallel to the axis of the aperture, and ρ_0 is the distance between the aperture axis and the beam axis, as shown in the Figure 3.2. Using ρ_0/a we can express this distance in a convenient ratio, where $\rho_0/a = 0$ implies that both the axis coincide, and $\rho_0/a = 1$ implies that both the axes are a radius a away from each other.

The central region of the $\ell = 4$ beam was overexposed to see the minima better.

3.4 Results and conclusions

3.4.1 Centered incident beam

The diffraction of LGV beams from a circular aperture produced concentric rings centered on the beam axis. This pattern has a circular symmetry. As an example, the diffraction pattern of $\ell = 1$ at $a/w = 0.2$ is shown in Figure 3.5. The intensity of the centeral ring of the diffraction pattern was much larger than the intensity of the outer rings. To see the fainter outer rings clearly the camera was deliberately overexposed. The camera's sensor around the central ring was saturated, which is seen as a plateau in the experimental graph.

The experimental intensity values of the diffraction pattern were extracted by taking the center of the central dark spot as the origin and scanning in the radial direction, as

shown by the line in Figure 3.5. To find the center of the diffraction pattern the images were imported into Mathematica. A smoothing transformation was applied to the image data before using an algorithm with an initial value of position to find the local minima around that position. The dots are the intensity values extracted from the image obtained from the CCD, by scanning from the center along the radial direction of the diffraction pattern. The continuous line in the 2D plot is the theoretical curve computed from Equation 3.7. To match the theoretical and experimentally recorded intensity profiles, one of the theoretically calculated intensities was scaled to match the corresponding experimental intensity. No other fitting parameters were used. The procedure is similar to the one used in the previous chapter for a single slit diffraction.

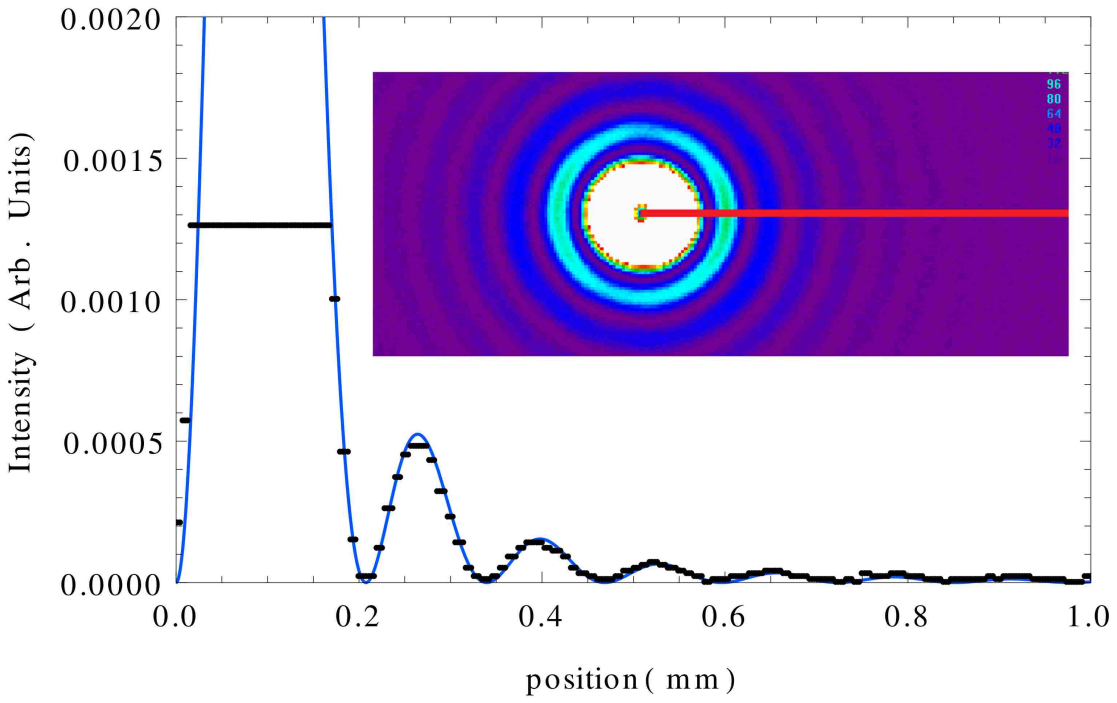

Figure 3.5: Diffraction at a 500μm aperture, for $\ell = 1$ LGV beam, with $a/w = 0.2$. The Blue line is the numerically calculated pattern, the black dots are the experimental data scanned from the inset picture, the original image, the red line shows the direction of the pixel wide scan to obtain the experimental data.

When the aperture size is larger than the beam size, i.e, a/w larger than 1, the central ring was very bright and the outer rings were very faint. In Figure 3.6 the image on the left is the experimentally recorded diffraction pattern for $a/w = 1.2$ when $\ell = 3$ LGV beam is diffracted by a 500μm aperture. Here we can see the intensity difference between the central ring and the faint outer rings. A single pixel wide scan in the radial direction shows small irregular bumps where the rings should for the first few outer rings. As we go further away from the center, a single pixel wide scan on these outer rings looks like noise as every pixel in the ring region does not capture the light. Nonetheless the rings were visible when viewing the entire image, as oposed to a single row, but were faint. To increase the visibility of these rings, a new image was created by importing the experimental image as a matrix into Mathematica and taking the logarithm of the experimentally recorded Intensity values. Doing this, made the fainter rings brighter than before. Note this was done to increase the visibility of the rings and not to measure the intensity values. Figure 3.6 shows a recorded diffraction pattern versus the new image created by taking the logarithm of the original experimental image. The overlay plot on the right hand side is the transverse profile of the numerically calculated diffraction pattern.

In a few cases, for example when $a/w = 1.2$ and $\ell = 2$, as shown in Figure 3.7, a predicted minima was within the experimentally recorded bright ring plateau. This could not be resolved by the camera, as the central ring intensity was very large.

The diffraction patterns for $\ell \neq 0$ are different from the Airy diffraction pattern. We observe that the position of the zeros of the diffraction pattern depend on the angular momentum of the incident field. The minima of the diffraction of LGV beam of order ℓ depends on $\ell + 1$ order Bessel function as predicted by the calculations. Further it was

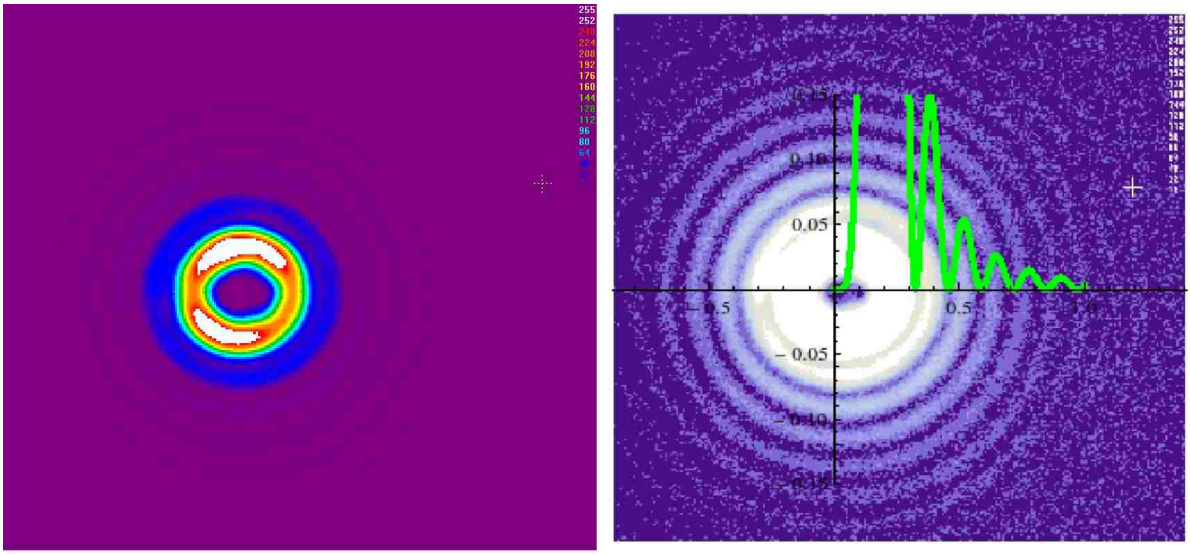

Figure 3.6: Diffraction at a 500μm aperture, for $\ell = 3$ LGV beam, with $a/w = 1.2$. The left is the experimentally recorded image, the right is the image created by taking the logarithm of the recorded image, the line is the transverse profile of the numerically calculated diffraction pattern

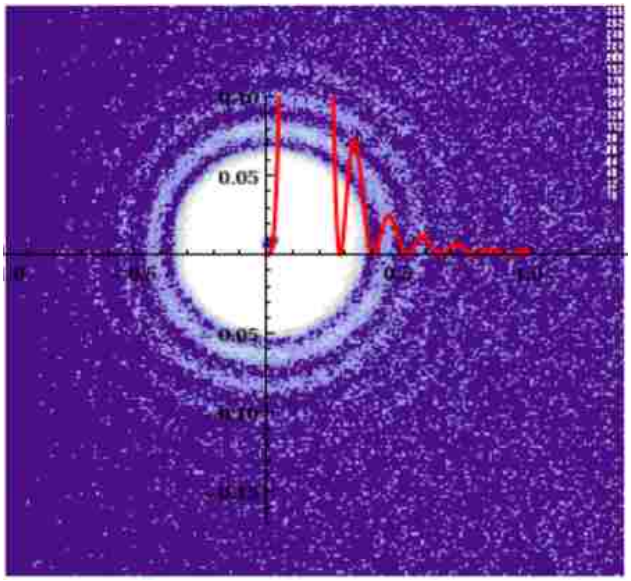

Figure 3.7: Diffraction at a 500μm aperture, for $\ell = 2$ LGV beam, with $a/w = 1.2$. The green line is the transverse profile of the numerically calculated diffraction pattern. The predicted minima is within the experimentally recorded bright ring plateau. The central ring intensity was too large and minima could not be resolved.

found that the diffraction patterns do not depend on the sign of the topological charge. $J_{-\ell}(x) = (-1)^{\ell} J_{\ell}(x)$, the intensity pattern as expected from Equation 3.8 will remain the same for $\pm\ell$.

Plotting the radial position of the minima or zeros of the diffraction pattern as a function of a/w we observe that, the radial position of each zero with respect to the beam axis increases, as a/w increases. This effect is more pronounced for the first few zeros. This can be seen in the Figure 3.8, where $\ell = 0$ and $\ell = 3$ cases are shown. The overlayed plot is the transverse diffraction pattern for $\ell = 3$ for $a/w = 0.2$. This is done to clarify what the y-axis is, on the graphs.

As the order of the LGV beams increases, there are two features that are observed. As ℓ increases, the position of the zeros from the beam axis increases, and the rate of change of the position of the zeros with respect to a/w from the beam axis decreases. This can be seen in Figure 3.8. For $\ell = 0$ the first minimum shows an increase in the minimum's position as a/w increases, but the first minimum in the $\ell = 3$ graph shows a less pronounced increase.

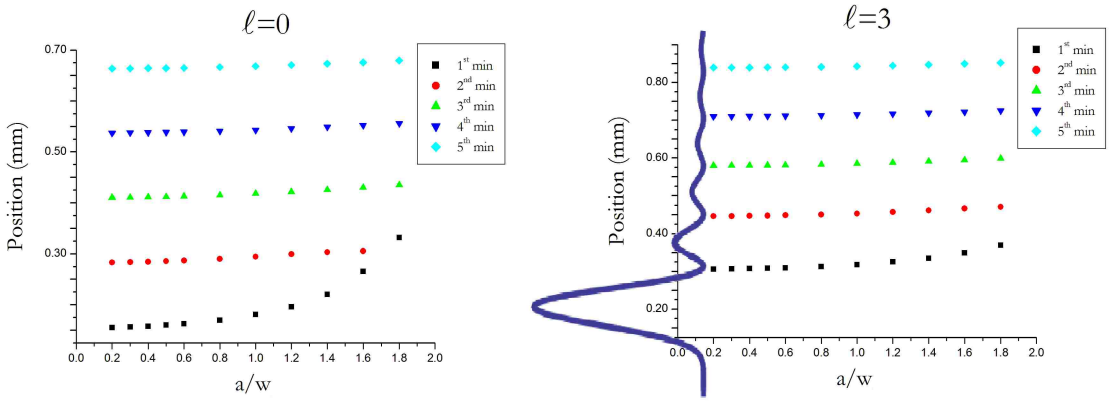

Figure 3.8: The positon of the zeros of the diffraction pattern are plotted as a function of a/w for $\ell = 0, 3$ the blue line is the transverse diffraction pattern for $\ell = 3$ for $a/w = 0.2$ to clarify the y-axis on the graphs.

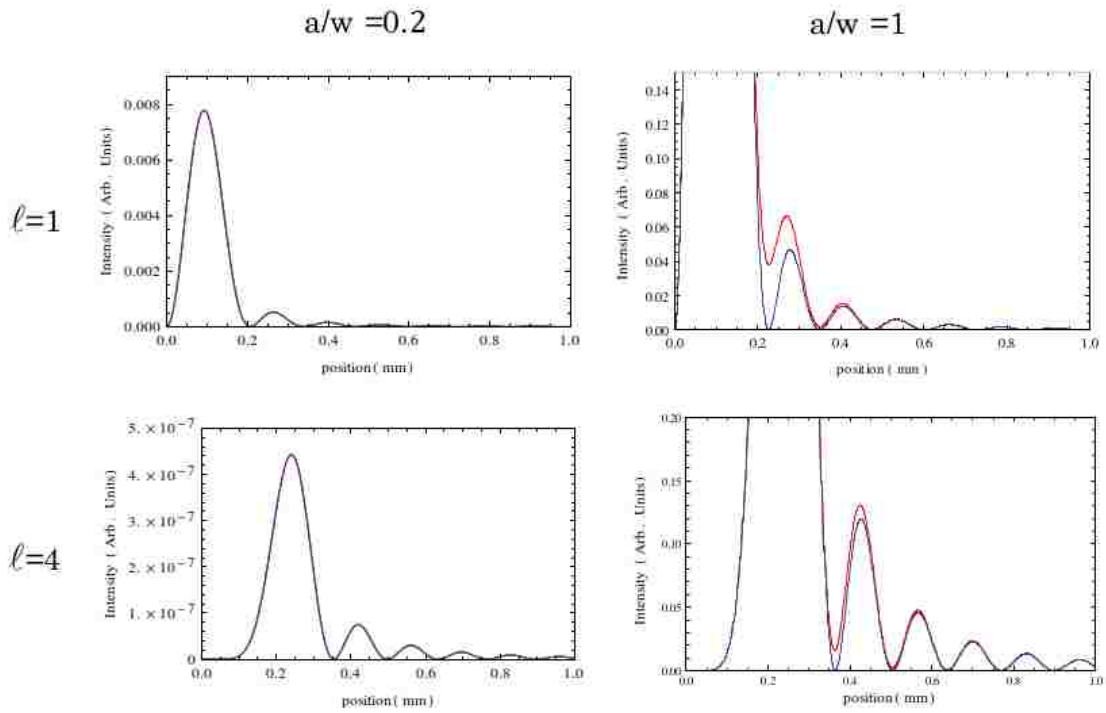

Figure 3.9: At $a/w = 0.2$ the diffraction patterns at the waist and at the Rayleigh range overlap completely, as the a/w ratio increases the patterns start to deviate as seen at $a/w = 1$

To study the effect of curvature of the phase front of the incident beam on the diffraction pattern, we placed the aperture a distance equal to one Rayleigh range away from the waist, that is at $z = z_R$ and $z = -z_R$ from the waist position. Comparing the diffraction pattern here, with the diffraction pattern at the waist, we observe that the minima occur at the same positions, but the intensity is non zero. The difference in intensities between the second maximum and the first minimum is smaller at the Rayleigh range than at the waist. As the radius of the aperture becomes larger compared to w, this effect becomes more pronounced as seen for $a/w = 1$, and at lower values of a/w, the minima of the diffraction pattern is close to zero, as seen for $a/w = 0.2$, in Figure 3.9. We also observe that this effect becomes less pronounced as the order of LGV beams increases, as can be seen when comparing the $\ell = 1$ pattern with the $\ell = 4$ pattern at the Rayleigh

range. The red line is the diffraction pattern at the Rayleigh range, and the blue line at the waist.

3.4.2 Misaligned aperture diffraction

The effect of misalignment of the aperture is studied. The diffraction patterns of the $\ell = 1$ order LGV beam with various ρ_0/a ratios are seen in Figure 3.10. The experimentally recorded images are on the top row, and the theoretically calculated intensity patterns are on the bottom row. Here, we see that the central minimum moves away from center of the diffraction pattern as the beam axis moves away from the aperture axis. There is only one minimum for $\ell = 1$.

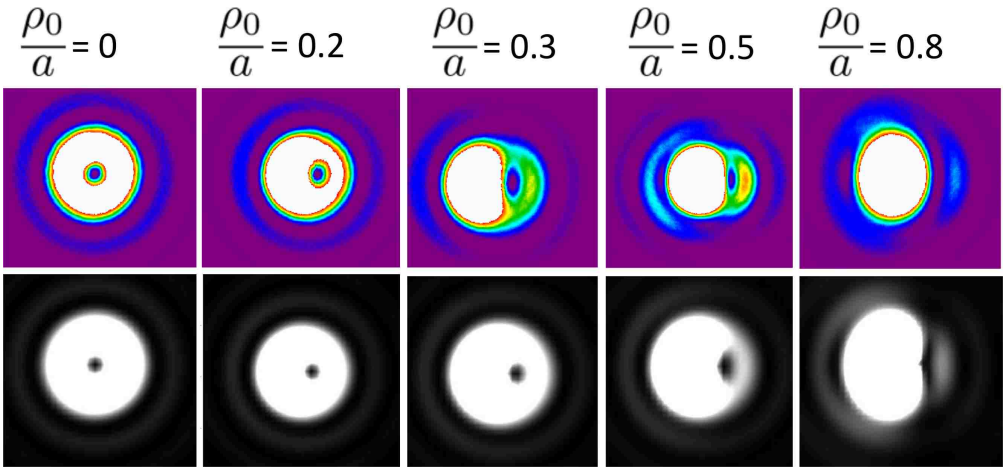

Figure 3.10: Diffraction pattern for $\ell = 1$ LGV beam when the beam axis is displaced. The top row shows the experimentally recorded patterns, and the bottom row shows the theoretically calculated patterns.

For $\ell = 2$ as seen in Figure 3.11, there are two minima and they move away from the center of the diffraction pattern as ρ_0/a increases. In addition to that, we notice an important property that was not noticeable with just the diffraction patterns of $\ell = 1$. The number of minima when we move away from $\rho_0/a = 0$ equals the order of the LGV beam.

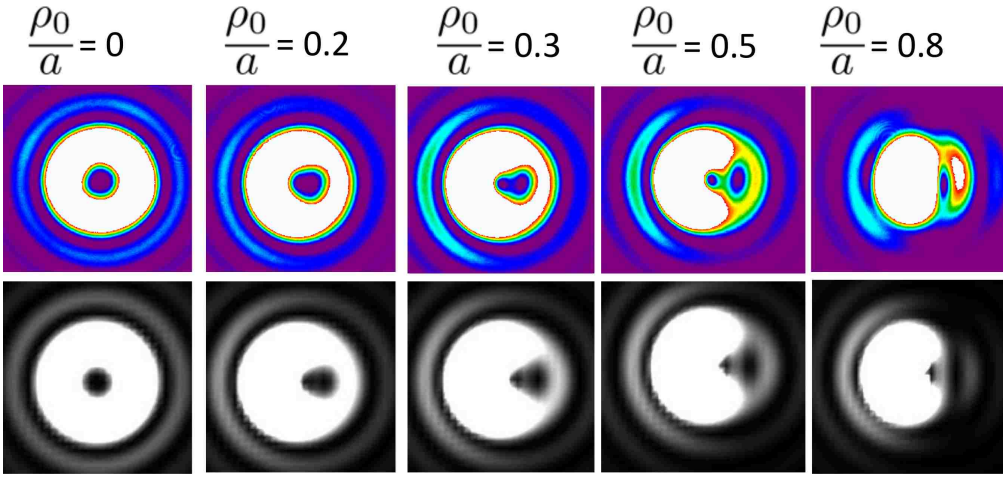

Figure 3.11: Diffraction pattern for $\ell = 2$ LGV beam when the beam axis is displaced. Two minima are visible when the ratio $\rho_0/a > 0$ The top row shows the experimentally recorded patterns, and the bottom row shows the theoretically calculated patterns.

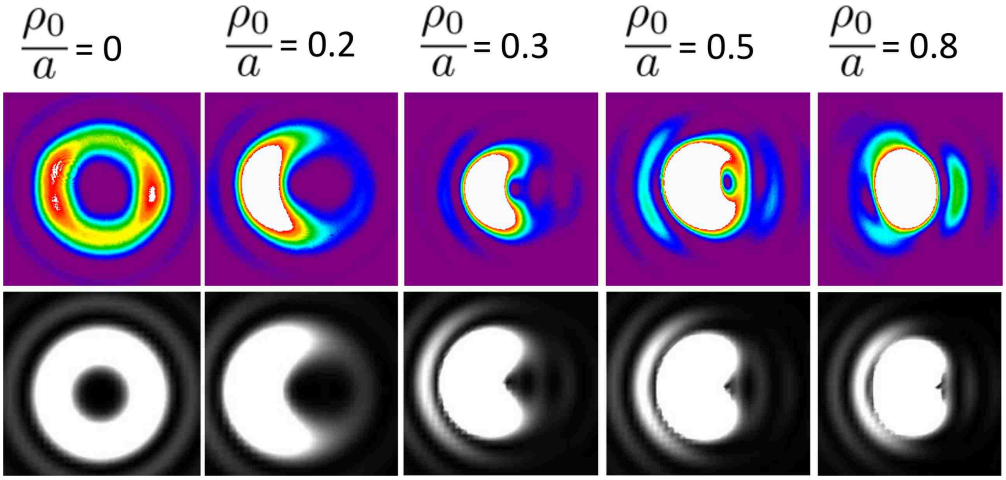

Figure 3.12: Diffraction pattern for $\ell = 3$ LGV beam when the beam axis is displaced. Three minima are visible when the ratio $\rho_0/a > 0$ The top row shows the experimentally recorded patterns, and the bottom row shows the theoretically calculated patterns.

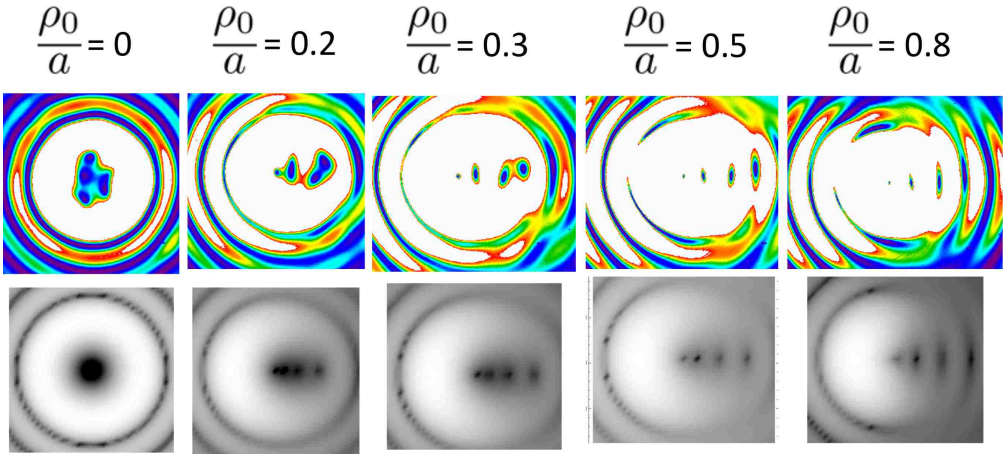

Figure 3.13: Diffraction pattern for $\ell = 4$ LGV beam when the beam axis is displaced. Four minima are visible when the ratio $\rho_0/a > 0$ The top row shows the experimentally recorded patterns, and the bottom row shows the theoretically calculated patterns.

This pattern continues in the diffraction pattern of $\ell = 3$ and $\ell = 4$ as can be seen in Figures 3.12 and 3.13, respectively.

In the theoretical calculations of $\ell = 4$, the difference between the minima and the maxima intensities was too small to resolve the sucessive minima positions well. Thus, the theoretical image for $\ell = 4$ is a logarithm of the theoretical intensity values, to show the position of the minima with higher resolution.

The minima move away from the center in a straight line as the ratio ρ_0/a increases. The first minimum moves less when compared to the second, which moves less compared to the third and the fourth moves the fastest. Figure 3.14 shows the plots of distance the minima moved from the center on the y axis, versus the ρ_0/a ratio which signifies how far away the beam axis is from the aperture axis. The y axis scale is not the same for each of the plots. The theoretical line is a spline curve fitting for the minima positions of the diffraction pattern obtained for various values of ρ_0/a. The dots and squares represent the experimental minima obtained from the images. In this study, the diffraction of the LGV

beam was studied at the waist of the beam, to observe the effect of misalignment.

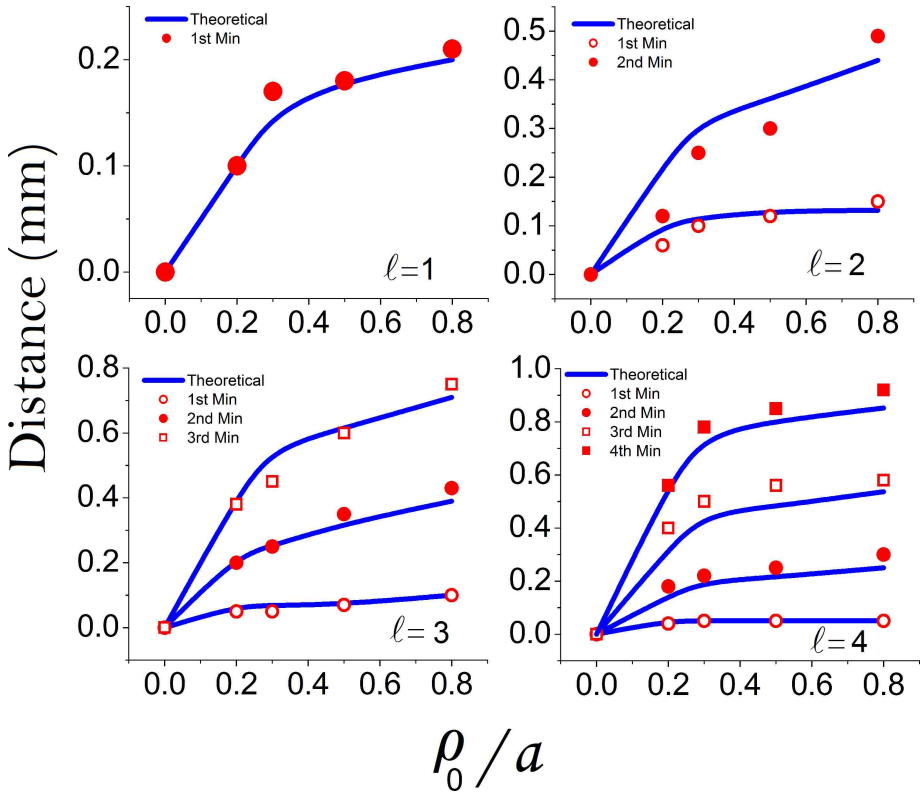

Figure 3.14: Plots of minima position vs ρ_0/a

In conclusion, the diffraction of LGV beams by a circular aperture has been studied. The minima of the diffraction of LGV beams of order ℓ depend on the $\ell + 1$ order Bessel functions. The diffraction pattern does not depend on the sign of the topological charge. As the radius of the aperture becomes large compared with the waist spot size, the distance of the zeros from the beam axis increases. It is found that, as the order of the LGV beam increases, the rate of change of the position of the zeros with respect to a/w from the beam axis decreases. The curvature of the beam also affects the diffraction pattern. The effect becomes more pronounced for larger a/w and lower ℓ.

The effects of misalignment, when the beam axis parallel to the aperture axis but laterally displaced, for a circular aperture was also studied. The number of minina seen

when $\rho_0 > 0$ is the order of the LGV beam. As the separation between the beam axis and the aperture axis increases, the separation of the minima increases as well.

Chapter 4

Polygonal Aperture Diffraction

4.1 Introduction

Diffraction of plane waves by polygons was studied in 1980s [34, 35]. Diffraction of Laguerre Gaussian vortex (LGV) beams by polygons had not been studied until recently [20, 21, 36]. There was an attempt at studying the diffraction of a circular aperture by LGV beams, but a 11 sided iris was used in the experiment [21], which resulted in a diffraction pattern that of a 11 sided polygon instead. The diffraction of LGV beams by a triangular aperture resulted in a triangular optical lattice [20, 36].

The diffraction of the fundamental gaussian beam by regular polygon of n sides, referred to as a regular $n-$gon, has a $2n-$fold symmetry for odd n, and an $n-$fold symmetry for even n. This symmetry is not expected in the the diffraction of LGV beams as the phase varies across the aperture. In Figure 4.1, the picture on the left shows the diffraction pattern of a plane wave when incident on a triangular aperture, and the picture on the right shows the diffraction pattern of an LGV beam of order $\ell = 1$ when diffracted by a triangle.

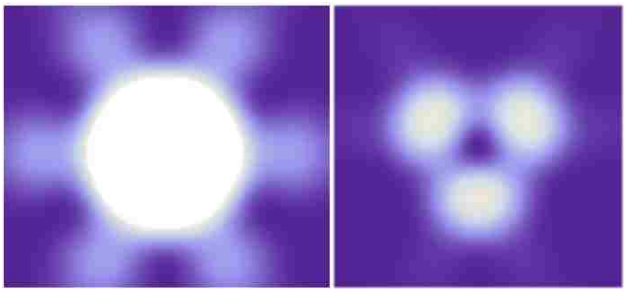

Figure 4.1: Diffraction patterns due to a triangular aperture. The picture on the left is when a plane wave is diffracted, and the picture on the right shows the diffraction pattern of an LGV beam of order $\ell = 1$.

In this study we describe new features in the far field diffraction pattern of LGV beams, when they are diffracted by regular polygons. These features depend on the orbital angular momentum index ℓ of the beam, the number of sides n of the polygon, and location of the aperture relative to the waist of the incident beam. We describe experiments, which reveal these new features and study their evolution as angular momentum index ℓ of the beam and the location of the aperture relative to the waist of the incident beam are varied along the direction of propagation.

4.2 Theory

The Fraunhofer diffraction is given by the fourier transform

$$U_f(x,y) = \frac{ik}{2\pi f}\iint_A dA U_{in}(x',y',z)e^{-\frac{ik}{f}(xx'+yy')}. \tag{4.1}$$

Here the input beam $U_{in}(\rho',\phi',z)$ is an LGV beam of order ℓ. In the cylindrical coordinates,

$$U_{in}(\rho',\phi',z) = C_\ell\left(\frac{\sqrt{2}\rho' e^{i\phi'}}{w}\right)^\ell \exp\left[-\frac{\rho'^2}{ww_0}e^{-i\theta(z)} + ik(z-z_0) - i(\ell+1)\theta(z)\right], \tag{4.2}$$

where the primed quantities are in the aperture plane, and the unprimed quantities are in the observation plane. C_ℓ is a consant. z_0 is the position of the waist, $\theta(z) = tan^{-1}((z-zo)/z_R)$, and z_R is the Rayleigh range.

C_ℓ along with $\exp[ik(z-z_0) - i(\ell+1)\theta(z)]$ can be absorbed into C'_ℓ as they do not depend on ρ' or ϕ' , thus

$$U_{in}(\rho',\phi',z) = C'_\ell\left(\frac{\sqrt{2}\rho' e^{i\phi'}}{w}\right)^\ell \exp\left[-\frac{\rho'^2}{ww_0}e^{-i\theta(z)}\right]. \tag{4.3}$$

For LGV beam diffraction the above diffraction integral in cylindrical coordiantes is

$$U_f^\ell(\rho,\phi) = C'_\ell \iint_A dA \left(\frac{\sqrt{2}\rho' e^{i\phi'}}{w}\right)^\ell \times \exp\left[-\frac{ik}{f}\rho\rho'\cos(\phi-\phi') - \frac{\rho'^2}{ww_0}e^{-i\theta(z)}\right]. \quad (4.4)$$

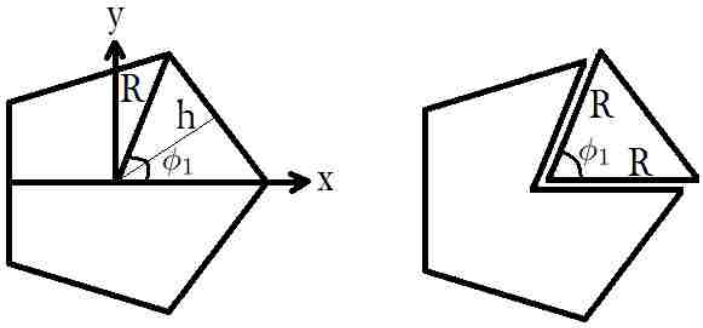

Figure 4.2: The left polygon shows the coordinate system and the parameters R, h, and the variable ϕ used in the calculations. The figure on the right shows a slice of a isosceles triangle created with the edge of the polygon and the two segments of length R from the center of the polygon to its vertices.

To find the area of integration A for the n sided regular polygon, let the angle subtended by the line segment connecting two adjacent vertices and the center be $\phi_k = \frac{2\pi}{n}k$, where $k = 0, 1, 2, \cdots (n-1)$ and $\rho_{max}(\phi') = \frac{h}{\cos(\phi' - \phi_{k+\frac{1}{2}})} = \frac{R\cos(\pi/n)}{\cos(\phi' - \phi_{k+\frac{1}{2}})}$ is the length of the segment connecting the center to the edge of the polygon, it has a maximum value of R, and a minimum value of h.

The integral $U_f^\ell(\rho,\phi)$ can be written as summation of the integrals over the isosceles triangles created by the edge of the polygon and the two segments R from the center of the polygon as shown in Figure 4.2. Thus,

$$U_f^\ell(\rho,\phi) = C'_\ell \sum_{k=0}^{n-1} \int_{\phi_k}^{\phi_{k+1}} d\phi' e^{i\ell\phi'} \int_0^{\rho_{max}(\phi')} \rho' d\rho' \left(\frac{\sqrt{2}\rho'}{w}\right)^\ell \times \exp\left[-\frac{ik}{f}\rho\rho'\cos(\phi-\phi') - \frac{\rho'^2}{ww_0}e^{-i\theta(z)}\right]. \quad (4.5)$$

To evaluate this integral we will need a series of substitutions. We begin with a

substitution $\psi = \phi' - \phi_{k+\frac{1}{2}}$ so that $\phi' = \psi + \phi_{k+\frac{1}{2}}$. When $\phi' = \phi_k$, $\psi = \phi_k - \phi_{k+\frac{1}{2}}$. The angle between ϕ_k and ϕ_{k+1} is $\frac{2\pi}{n}$, thus the angle between ϕ_k and $\phi_{k+\frac{1}{2}}$ is $\frac{\pi}{n}$. The limits now vary from $-\frac{\pi}{n}$ to $\frac{\pi}{n}$.

Using the substitution and the new limits the integral can be written as,

$$U_f^\ell(\rho,\phi) = C'_\ell \sum_{k=0}^{n-1} \int_{-\pi/n}^{\pi/n} d\psi e^{i\ell\psi} e^{i\ell\phi_{k+\frac{1}{2}}} \int_0^{\rho_{max}(\phi')} \rho'^{\ell+1} d\rho' \left(\frac{\sqrt{2}}{w}\right)^\ell \times \exp\left[-\frac{ik}{f}\rho\rho'\cos(\psi + \phi_{k+\frac{1}{2}} - \phi) - \frac{\rho'^2}{ww_0}e^{-i\theta(z)}\right]. \tag{4.6}$$

Next, we make the substitution $A = \dfrac{e^{-i\theta}}{ww_0}$ and $B = \dfrac{k\rho}{f}\cos\left(\psi + \phi_{k+\frac{1}{2}} - \phi\right)$. The integral can be simplified to

$$U_f^\ell(\rho,\phi) = C'_\ell \sum_{k=0}^{n-1} \int_{-\pi/n}^{\pi/n} d\psi e^{i\ell\psi} e^{i\ell\phi_{k+\frac{1}{2}}} e^{-\frac{B^2}{4A}} \int_0^{\rho_{max}(\phi')} \rho'^{\ell+1} d\rho' \left(\frac{\sqrt{2}}{w}\right)^\ell \times \exp\left[-A\left(\rho' + \frac{iB}{2A}\right)^2\right]. \tag{4.7}$$

Now to evaluate the ρ' part of the integral, write $U_f^\ell(\rho,\phi)$ as

$$U_f^\ell(\rho,\phi) = C'_\ell \sum_{k=0}^{n-1} \left(\frac{\sqrt{2}}{w}\right)^\ell \int_{-\pi/n}^{\pi/n} d\psi e^{i\ell\psi} e^{i\ell\phi_{k+\frac{1}{2}}} e^{-\frac{B^2}{4A}} \times I(\rho,\phi,\psi), \tag{4.8}$$

where,

$$I(\rho,\phi,\psi) = \int_0^{\rho_{max}(\phi')} \rho'^{\ell+1} d\rho' \exp\left[-A\left(\rho' + \frac{iB}{2A}\right)^2\right]. \tag{4.9}$$

$I(\rho,\phi,\psi)$ can be rewritten by making the substitution $X = \sqrt{A}\left(\rho' + \dfrac{iB}{2A}\right)$ and using the binomial expansion $(x+y)^n = \sum_{k=0}^n C_k^n x^k y^{n-k}$. This changes the limits of integration to

$X_0 = \dfrac{iB}{2\sqrt{A}}$ and $X_{max} = \dfrac{\sqrt{A}h}{\cos\psi} + \dfrac{iB}{2\sqrt{A}}$. The integral now has the form

$$I(\rho,\phi,\psi) = \frac{1}{\sqrt{A}} \sum_{m=0}^{\ell+1} C_m^{\ell+1} \left(\frac{-iB}{2}\right)^{\ell+1-m} \left(\frac{1}{A}\right)^{\ell+1-m} \left(\frac{1}{\sqrt{A}}\right)^{m} \int_{X_0}^{X_{max}} X^m e^{-X^2} dX. \quad (4.10)$$

Using this expression for $I(\rho,\phi,\psi)$ and absorbing the constants into C'_ℓ we obtain,

$$U_f^\ell(\rho,\phi) = C'_\ell \sum_{k=0}^{n-1} \left(\frac{\sqrt{2}}{w}\right)^{\ell} e^{i\ell\phi_{k+\frac{1}{2}}} \left(\frac{1}{\sqrt{A}}\right) \sum_{m=0}^{\ell+1} C_m^{\ell+1} \left(\frac{-i}{\sqrt{A}}\right)^{\ell+1-m} \int_{-\pi/n}^{\pi/n} d\psi e^{i\ell\psi} GI_m, \quad (4.11)$$

where,

$$GI_m = \int_{X_0}^{X_{max}} X^m e^{-X^2} dX. \quad (4.12)$$

To evaluate GI_m, we use the following Gaussian integrals:

$$\int x^{2r+1}\varphi(x)dx = -\varphi(x) \sum_{j=0}^{r} \frac{(2r)!!}{(2j)!!} x^{2j} + c, \quad (4.13)$$

$$\int x^{2r+2}\varphi(x)dx = -\varphi(x) \sum_{j=0}^{r} \frac{(2r+1)!!}{(2j+1)!!} x^{2j+1} + (2r+1)!!\Phi(x) + c. \quad (4.14)$$

Here, $\varphi(x) = \dfrac{e^{-\frac{x^2}{2}}}{\sqrt{2\pi}}$, the cumulative distribution $\Phi(x) = \frac{1}{2}\left(1 + \mathrm{erf}\left(\frac{x}{\sqrt{2}}\right)\right)$, and c is the constant of integration in these indefinite integrals [30].

We can now write $\varphi(\sqrt{2}X) = \dfrac{e^{-X^2}}{\sqrt{2\pi}}$ and evaluate GI_m. If $m = 2r+1$, then

$$GI_{odd} = \left[-\frac{e^{-X^2}}{2^{r+1}} \sum_{j=0}^{r} 2^j \frac{(2r)!!}{(2j)!!} X^{2j} \right]_{X_0}^{X_{max}}, \quad (4.15)$$

and if $m = 2r + 2$, then

$$GI_{even} = \left[-\frac{e^{-X^2}}{2^{r+1}} \sum_{j=0}^{r} 2^j \frac{(2r+1)!!}{(2j+1)!!} X^{2j+1} + \sqrt{2\pi}(2r+1)!!\Phi(\sqrt{2}X) \right]_{X_0}^{X_{max}}, \tag{4.16}$$

where $\Phi(\sqrt{2}X) = \frac{1}{2}(1 + \mathrm{erf}(X))$. Knowing the expression for GI_m, we now have a suitable expression for the numerical evaluation of the diffracted field, $U_f^\ell(\rho, \phi)$.

When recalculating the indefinite form of the integral GI_m symbolically in Mathematica it resulted in an expression involving the upper incomplete Gamma function,

$$\int X^m e^{-X^2} dX = -\frac{1}{2} X^{m+1} (X^2)^{-\frac{m+1}{2}} \Gamma\left(\frac{m+1}{2}, X^2\right) + c. \tag{4.17}$$

The uppper incomplete Gamma function is an integral, but Mathematica does not evaluate this integral, instead it uses a precalculated table, thus considerably speeding up the numerical evaluation of the diffracted field; this speedup in most noticeable for higher order LGV beams.

4.3 Experiment

To study the diffraction of LGV beams by polygons we needed polygons that were of various sizes ranging form 50μm to about 400μm. The first attempt was made by using razor blades as edges of the polygons. This method was viable for lower order polygons, like triangles ($n = 3$), sqaures ($n = 4$) and pentagons ($n = 5$), but creating symmetric polygons of higher orders using razor blades became increasingly difficult.

There was a need to create polygonal apertures of various sizes. Using electron beam lithography these polygons were etched onto a glass plate that was coated with a thin layer of chromium, creating polygons inscribed inside a circle of diameter 50μm to 400μm. This

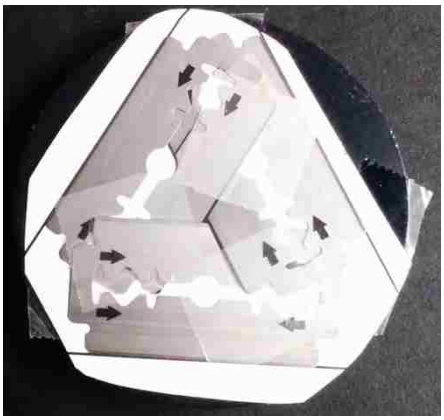

Figure 4.3: A triangular aperture made with razor blades.

glass plate was designed by Dr. Rob Sleezer and was fabricated by Advance Reproductions, an e-beam lithography company in Andover, MA.

The LGV beams produced using the method described in Chapter 1 was used in this experiment. Here is a summary of the method. The He:Ne laser cavity was used to produce HG beams. A maximum order of 4 was produced by introducing cross fibers that created a loss in the cavity. The HG modes were passed through an astigmatic mode converter, and LGV beams were produced. With a maximum order HG_{04} mode, an LGV beam of order $\ell = 4$ could be produced using this method. We also needed higher order LGV beams.

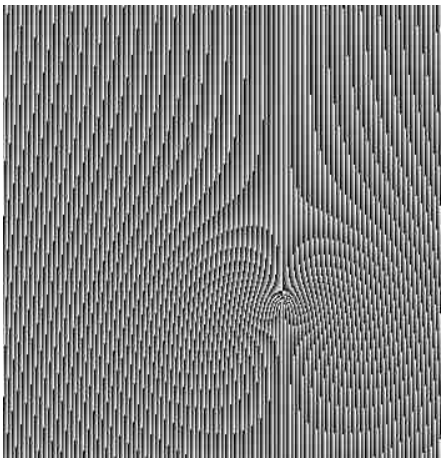

Figure 4.4: Blazed fork grating used to create $\ell = 10$ LGV beam.

To create higher order LGV beams, a reflective phase only spatial light modulator (SLM) was used. Collimated HG_{00} mode from a He:Ne laser was incident on the SLM. Having a blazed fork gratting pattern similar to that shown in Figure 4.4 on the SLM, the HG_{00} mode was converted to an LGV beam. These modes were created with the help of Sean Nomoto, who is well versed with the use of an SLM. The pattern shown in Figure 4.4 was used to create an LGV beam of order $\ell = 10$.

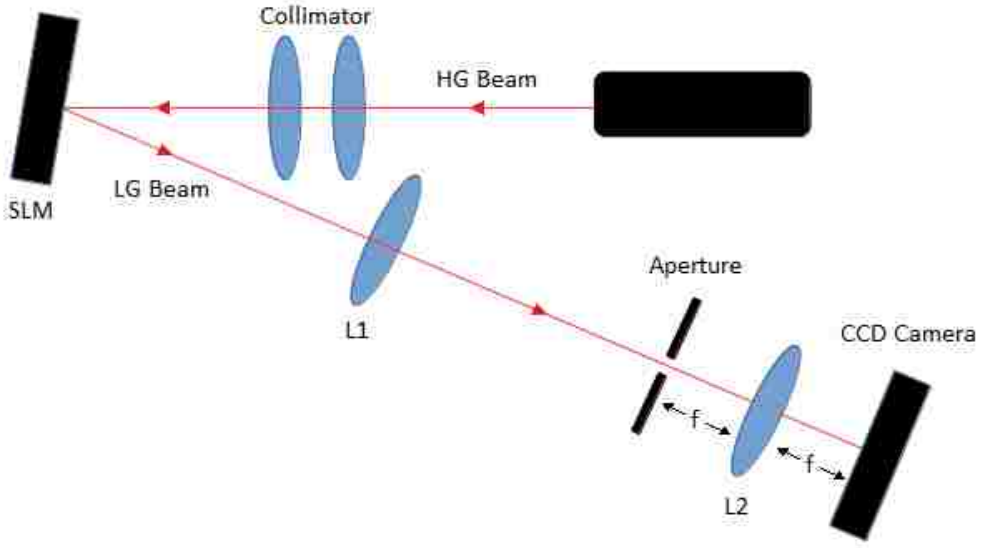

Figure 4.5: A schematic diagram of the setup used to covert HG_{00} to LGV beams and study the diffraction of the LGV beams once created. A collimator is used to collimate the incident HG_{00} mode. Lens L1 is used to create a waist. The aperture, lens L2 and the CCD camera are in a $2f$ arrangement to study the far-field diffraction of LGV beams.

A schematic diagram of the experimental set up is shown in Figure 4.5. As the fork pattern can create both $\pm\ell$ LGV beams, a blazed fork grating was used to redirect most of the intensity towards $+\ell$ LGV beams.

The LGV beams produced in the SLM were then passed though lens L1 to create a waist. Changing the lens L1 with lens of different focal lengths, and varying its position we can create waists of different sizes. Lens with focal lengths from 35 cm to 75 cm were used

to create waists from 150 μm to 400 μm. As we used a collimated incident beam, the position of the waist produced with these different lens were close to the focal lengths of the lens, but a CCD camera was used to find the position of these waists experimentally.

The aperture, and the CCD camera were a distance f from lens L2 of focal length f, in a $2-f$ arrangement, as described in Chapter 1. These three elements, the aperture, the lens L2, and the CCD camera constitute the detector block. The detector block was moved as a single unit, without changing the distance between the elements, to any position along the beam axis where the diffraction due to the aperture was studied.

The beam spot size w is the radius of a circle on the maximum intensity area of the LGV beam as shown in Figure 4.6.

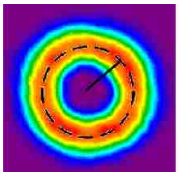

Figure 4.6: The radius w of the LGV beam of order ℓ, where w_0 is the size of the fundamental mode.

Figure 4.7 shows how the aperture size is varied with respect to the waist size. The top row shows $a/w = 1$ for a triangle, square and a pentagon. The radius of the circle in which the polygon is inscribed is a, and the waist radius is w. The bottom row shows how the ratio a/w is changed by keeping the same aperture size, but by varying the beam size.

As the apertures were on a glass plate coated with a thin layer of chrome, this caused a light bleed through the glass plate in the plane of the aperture, when the beam spot size was larger than the aperture. This resulted in the input beam passing through the glass plate and being seen in the diffraction image superimposed on the diffraction pattern. As a

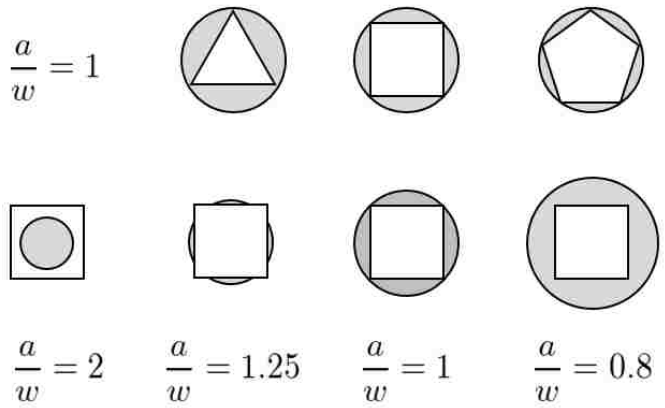

Figure 4.7: Top row shows triangle, square, and pentagon with $a/w = 1$. The bottom row shows a square with $a/w = 2, 1.25, 1, 0.8$

result of which the diffraction pattern could not be discerned. It is for this reason we stayed with $a/w \geq 1$ in this study.

The polygonal apertures with $n = 3 - 11$ were placed at the waist of the LGV beam and diffraction for $\ell = 1 - 12$ were observed.

4.4 Results and discussions

We look at the smaller order polygons first before moving on to the higher order polygons. Figure 4.8 shows the diffraction pattern produced by an equilateral triangle for LGV beams of order $\ell = 1 - 6$. The first major difference to note is that this being an odd $n-$polygon the diffraction pattern shows $n-$fold symmetry when diffracted by LGV beams, that is the diffraction pattern is triangular shape, though rotated by 30° which is half of the angle between the edges. This is unlike the $2n-$fold symmetry we see when a plane wave is diffracted by an odd $n-$polygon.

The number of maxima on the edge of the diffracted pattern is $\ell + 1$. The center of the diffracted pattern is dark except for the multiple of 3 order LGV beam. An examination of

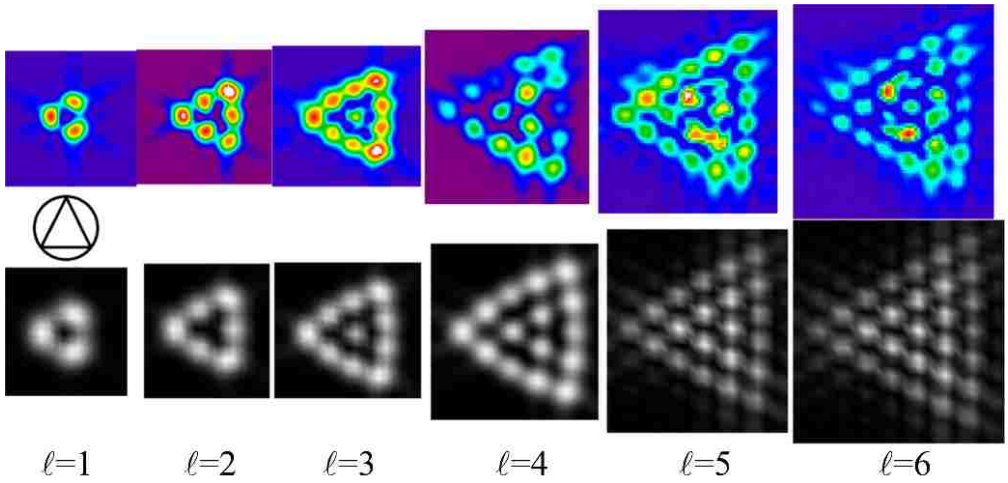

Figure 4.8: Diffraction images of various ℓ order LGV beams by a triangular aperture. The top row shows the experimentally obtained patterns, and the bottom row shows the theoretically calculated pattern. The experimental pattern are colored, and the theoretical patterns are black and white.

the phase over the edges is essential in understanding this phenomenon. The phase of the LGV beam varies over 6π for a $\ell = 3$ LGV beam. When a $\ell = 3$ LGV beam is incident on an equilateral triangle, there is a phase change of 2π over each edge. Any three equidistant points over the edges of the triangle, i.e one point on each edge and all three can make an equilateral triangle when connected, have the same phase, causing the diffracted light to constructively interfere in the center of the diffraction pattern. This can be seen for $\ell = 6$ as well, and indeed for all multiples of 3.

Next, we look at the diffraction pattern of $\ell = 4$ for a triangle. The outer edges have 5 maxima along the edge, but on the inside of this triangular ring of maxima, we can see the pattern of $\ell = 1$. This is true for all $\ell > n$. In the diffraction patterns of $\ell = 5$ and $\ell = 6$ we can see the patterns of $\ell = 2$, and $\ell = 3$ inside the first maxima edge boundary. The diffraction pattern is distinct for all $\ell \leq n$. For $\ell > n$ the diffraction pattern has a repeating structure. The diffraction patterns are analogues to the Matryoshka dolls, a

Russian nesting doll, where a bigger doll, has multiple smaller dolls within it.

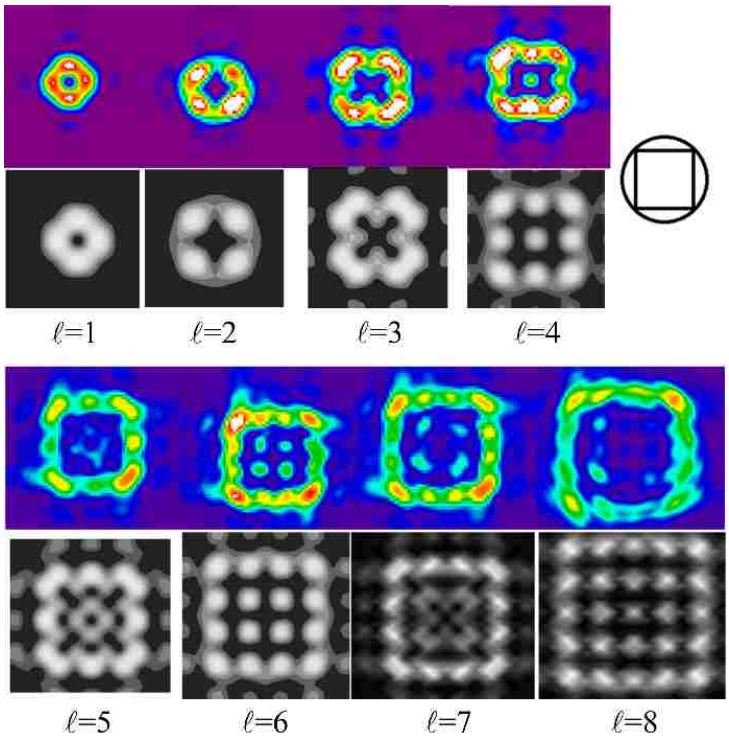

Figure 4.9: Diffraction patterns for a square (4−gon) for $\ell = 1 - 8$. The top row shows the experimentally obtained patterns, and just below them is the theoretically calculated pattern. The experimental pattern are colored, and the theoretical patterns are black and white.

This nesting diffraction pattern is not unique to triangles, but is exhibited in all polygons. The nesting starts to appear when the order of the LGV beam $\ell > n$. This can be seen in Figure 4.9 for a square.

The diffraction pattern for a pentagon is seen in the top half of Figure 4.10. The bottom half of Figure 4.10, shows the central bright spot in the diffraction patterns when $\ell = n$.

The diffraction of LGV beams by polygons creates an optical lattice. This lattice is more prominent for lower order polygons. As we reach $n \geq 5$ the lattice slowly starts becoming concentric rings, similar to the pattern of a circular aperture which has been described in chapter 3. LGV beam diffraction of lower order polygons could be used to

create optical traps.

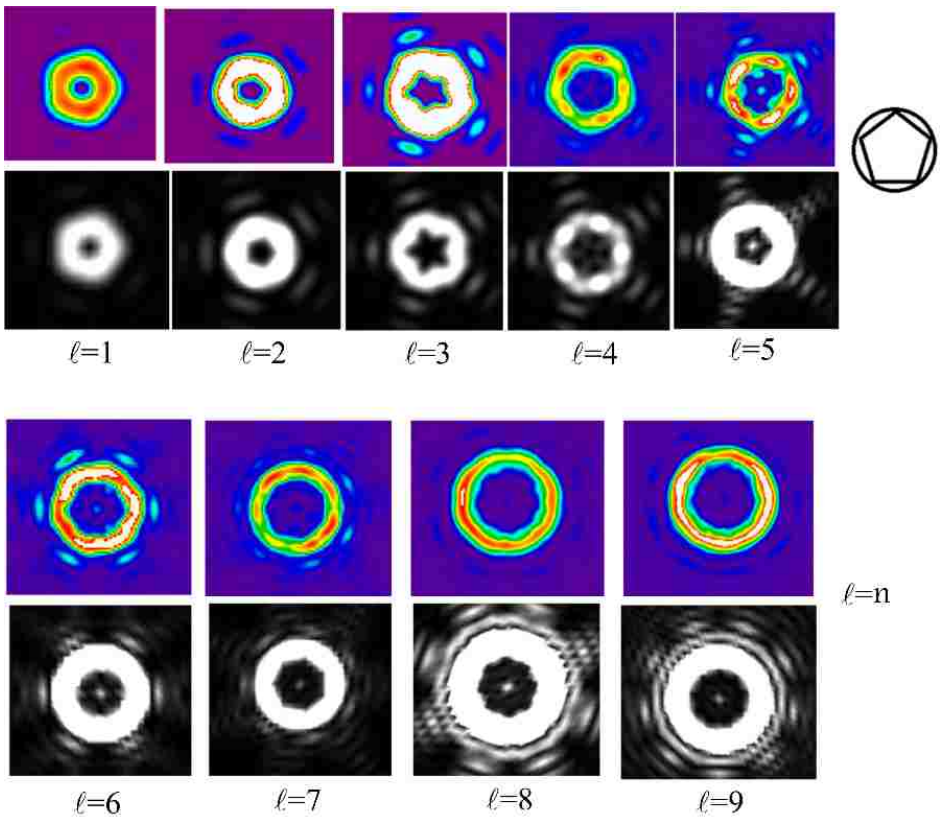

Figure 4.10: The top half shows the experimental(in color), and the theoretical patterns(black and white) of an LGV beam of orders $\ell = 1 - 5$ when diffracted by a pentagon. The bottom half shows the central bright sopt in the diffraction patterns when $\ell = n$.

When the aperture is not placed at the waist, there is a quadratic variation of the phase of the LGV beam. This causes a shear in the diffraction pattern when diffracted with polygons, similar to the shear caused when the LGV beams were diffracted with a slit as seen in chapter 2. Figure 4.11 shows the diffraction pattern and the shear that is experienced when a triangle and a square is diffracted by LGV beams at positions away from the waist along the beam propagation direction at Rayleigh range $z = \pm z_R$, and half Rayleigh range $z = \pm 0.5 z_R$. Maximum phasefront curvature of the beam occurs at the Rayleigh range, and we observe the maximum shear in the diffraction pattern at Rayleigh

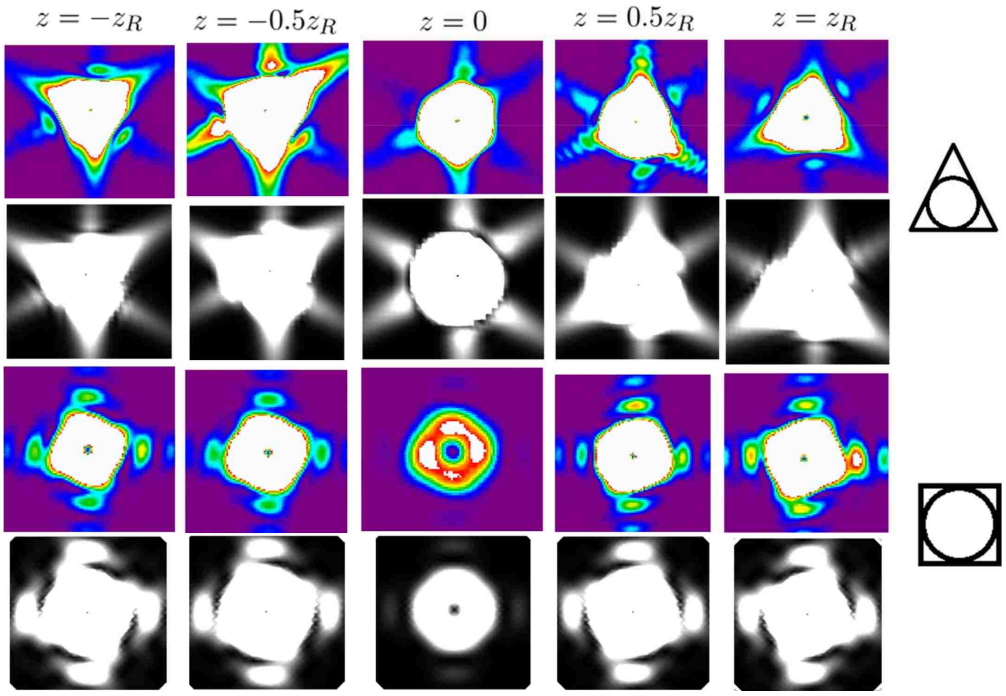

Figure 4.11: Experimental(color) and theoretical(black and white) shear patterns observed in the diffraction of LGV beam of order $\ell = 1$ by a triangular aperture on the top row, and by a square aperture in the bottom row as z varies.

range. Figure 4.12 shows the shear in the diffraction patterns of LGV beam of order $\ell = 1$ by a triangular aperture. In these images we can see the shear in the bright spots of the diffraction pattern at the Rayleigh range $z = z_R$, when compared to the pattern at the waist $z = 0$.

Shear patterns observed in the diffraction of LGV beam of order $\ell = 2$ by a triangular aperture on the top row, and by a square aperture in the bottom row as z varies are shown in Figure 4.13. The amount of shear is larger for $\ell = 2$ than that for $\ell = 1$. This effect is more prominent for larger ℓ as seen in Figure 4.14, where the diffraction patterns of LGV beams of order $\ell = 1 - 4$ when diffracted by a square is shown at the waist, one Rayleigh range after the waist, and one Rayleigh range before the waist.

In conclusion, Diffraction of LGV beams by a regular polygon results in a diffraction

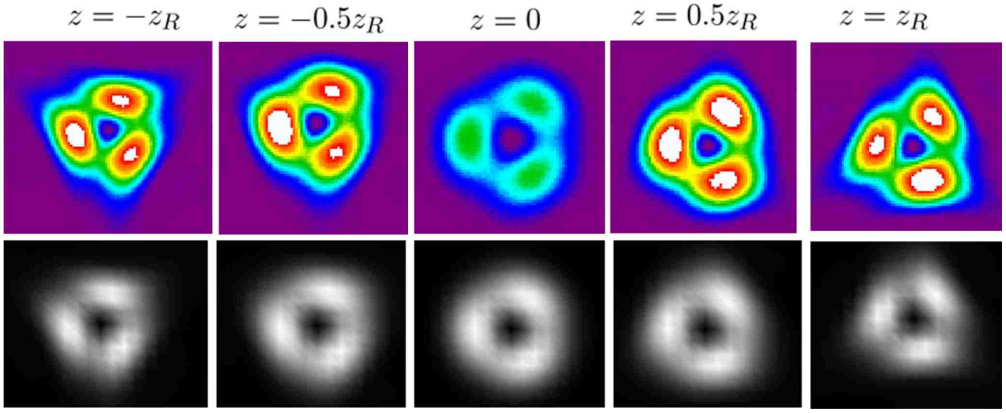

Figure 4.12: Experimental(color, top row) and theoretical(black and white, bottom row) shear patterns observed in the diffraction of LGV beam of order $\ell = 1$ by a triangular aperture as z varies.

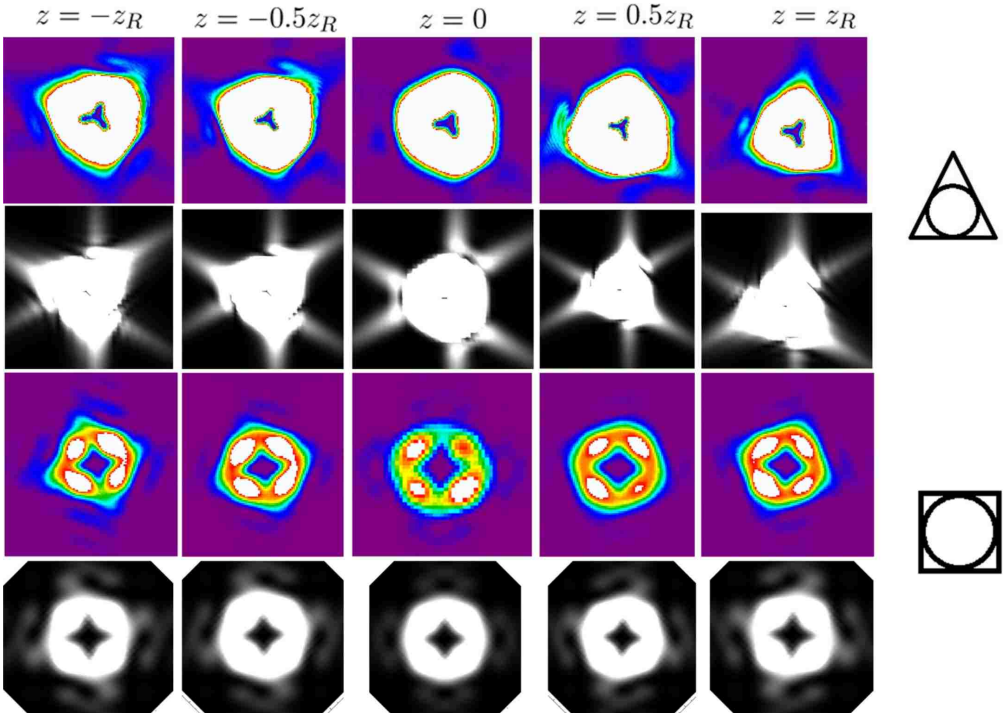

Figure 4.13: Experimental(color) and theoretical(black and white) shear patterns observed in the diffraction of LGV beam of order $\ell = 2$ by a triangular aperture on the top row, and by a square aperture in the bottom row as z varies.

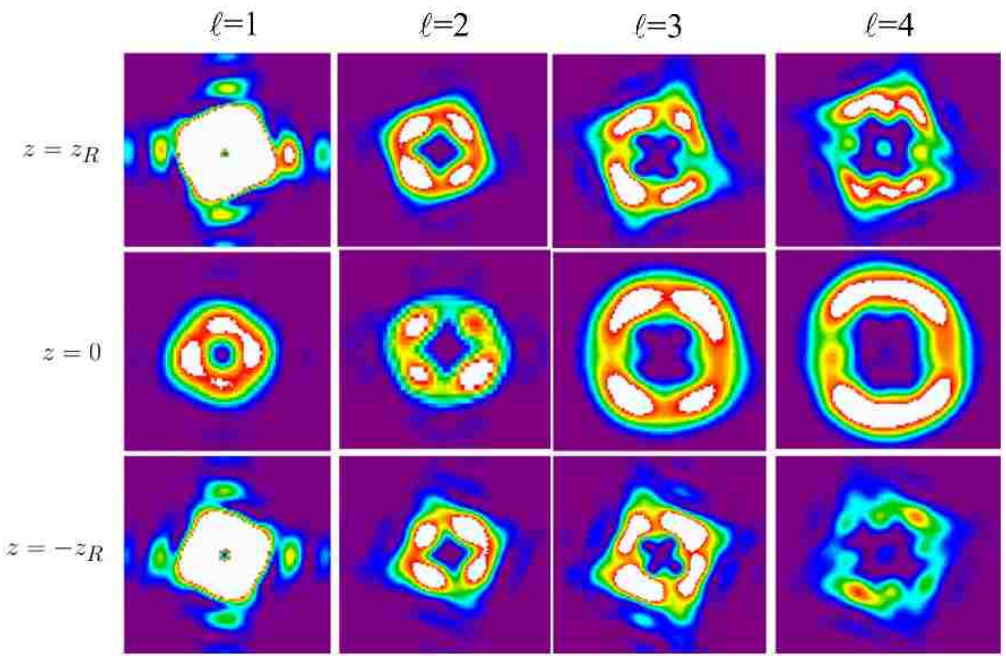

Figure 4.14: Experimental shear patterns observed in the diffraction of LGV beam of order $\ell = 1 - 4$ by a square aperture as z varies.

intensity pattern that is different from that made by the diffraction of a plane wave by regular polygons. The diffraction pattern of odd $n-$polygon has $n-$fold symmetry, unlike the $2n-$fold symmetry seen when diffracted by a plane wave. The center is bright when ℓ is a multiple of n. The diffraction pattern is distinct for all $\ell \leq n$. For $\ell > n$ the diffraction patterns has a repeating structure, similar to the russian Matryoshka nesting dolls. The shear in the diffraction pattern when the polygonal aperture is not at the waist is due to the curvature of the phasefront. The shear is more for higher ℓ.

Chapter 5

Conclusion

Diffraction plays an important role when there is an interaction of light and matter. The LGV beams carrying orbital angular momentum, have great potential for applications in many optical and telecommunication devices [12, 37]. The knowledge of the interaction of LGV beams with simple apertures will help advance the understanding of LGV beams and the creation of such devices. The diffraction of Laguerre Gauss Vortex (LGV) beam shows many novel features, that depend on the orbital angular momentum carried by the beam, the position of the aperture in the beam, and the ratio of the size of the aperture to the beam size. Obviously many of these features were not observed in the diffraction of plane waves and Hermite-Gaussian beams. We summarize the conclusions of this study, and give pointers to further research for understanding the optics of LGV beams.

5.1 Summary

The study began with the diffraction of LGV beams by a slit. It was found that for a planar phase front, i.e the aperture at the waist of the beam, the central diffraction maximum consists of $\ell + 1$ fringes, which are symmetrically located about the center of the pattern. Along the direction of propagation, at positions other than the waist, the phase front of the beam is curved. The angle of shear in the diffraction pattern depends on the sign of the radius of curvature $R(z)$ and the sign of the topological charge ℓ. The amount of shear in the diffraction pattern depends on the position of the aperture, with maximum shear at Rayleigh range. The sense of shear gives the sign of ℓ. It was also found that as

the slit is moved farther away from the waist ($\zeta \gg 1$), the diffraction pattern evolves into a pattern dominated by two peaks irrespective of ℓ.

The diffraction of the LGV beam by a circular aperture showed some new properties. The minima of the diffraction of LGV beams of order ℓ depends on the zeros of $\ell + 1$ order Bessel functions. The center of the diffraction pattern has a minimum for $\ell \geq 1$. Being circularly symmetric, the diffraction pattern does not depend on the sign of the topological charge. As the radius of the aperture becomes large compared with the waist spot size, the distance of the zeros of the diffraction pattern, from the beam axis increases. As the order of the LGV beam increases, the rate of change of the position of the zeros with respect to a/w from the beam axis decreases. The curvature of the beam also affects the diffraction pattern. The effect becomes more pronounced for larger a/w, and for lower ℓ. When the beam axis and the aperture axis are laterally separated, the central minimum of the diffraction pattern splits into a number of minina equal to the order of the LGV beam used. As the separation between the beam axis and the aperture axis increases, the separation of the minima increases as well.

The diffraction of LGV beams due to symmetric polygons leads to optical lattices. The diffraction pattern of odd $n-$polygon has $n-$fold symmetry, unlike the $2n-$fold symmetry seen, when diffracted by a plane wave. The center is bright when ℓ is a multiple of n. The diffraction pattern is distinct for all $\ell \leq n$. For $\ell > n$ the diffraction patterns has a repeating structure, similar to the russian Matryoshka nesting dolls.

5.2 Future Work

We have seen the effects of lateral misalignment of a circular aperture in Chapter 3. The effect of an angular misalignment, i.e a tilt must still be explored. For tilts $\theta \leq 15^\circ$ there does not appear to be a significant difference in the diffraction pattern, but this needs further investigation and modeling.

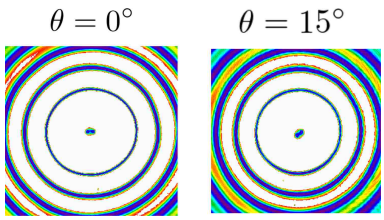

Figure 5.1: Diffraction pattern of LGV beams due to a circular aperture tilted at $\theta = 15^\circ$

As we saw in Chapter 4, diffraction of LGV beams by a polygon results in optical lattices, it is worthwhile to study the diffraction of periodic arrangement of apertures. This could result in nested periodic lattices or it may turn out to be highly dependent on symmetry of the arrangement of the apertures. This periodic arrangement can be done in two fundamental ways. The first way would be a periodic arrangement of apertures of similar sizes without overlap, for example a square on the vertices of a larger square, or larger triangle. Further study is required for the diffraction by overlapping apertures, either partially or completely nested, like the Sierpinski triangles [38].

Diffraction of LGV beams by soft apertures, apertures that do not have a well defined boundary but the transmission co-efficient of the edge gradually changes from 1 to 0 could be very useful in studying the effect of atmospheric turbulence with dust particles on LGV beams, as LGV beams are now under investigation to develop a better method for line of sight data transmission [39, 40]. This will need a closer look at the diffraction integral, as

the boundary conditions now are different and the transmission is no longer a step at the aperture boundary.

Diffraction of sub-wavelength apertures by beams carrying orbital angular momentum is worth investigating, not only because of the potential applications in telecommunication, but would also for discovering potentially new fundamental light matter interactions. It is proposed that the transmission through a slit array in an optically thick metal film is due to the excitation of 'coupled' modes on both the entrance and exit surfaces of the film and excitation of wave guide resonances within the slits themselves [41]. It would be interesting to see how the presence of orbital angular momentum affects these metal film array of apertures.

Intra-cavity generation of hight power LGV beams has been achieved, by the use of Q-plates but with very low effecieny [42], A pump beam of 100W of the fundamental HG mode was used to create 1W of LG beam. Creating high efficiency and high power intra-cavity LGV beams has not yet been achieved. Almost all methods used till date are lossy, or create a beam which is the superposition of $\pm\ell$ [43]. Creating miniature laser cavities that can create LG beams in a solid state material would be of interest in the telecommunication industry, as LGV beams are being studied as a replacement for gaussian beams in fibers [37]. Analogous to the nanolasers, where resonance in surface plasmons was used to create laser beams, it would be interesting to explore the idea of using surface plasmons for intra-cavity generation LGV beams [44, 45].

The orbital angular momentum in LGV beams can transfer angular momentum to an object, and can thus create a torque, this torque can be used in the study of single atom thick materials [46]. There are still many unexplored avenues in the study of LGV beams,

and its diffraction properties, which no doubt will continue to attract researchers for many years to come.

Appendix A

List of Publications

1. A. Ambuj, Hsiao harng Shiau, Michael Lucini, Reeta Vyas, and Surendra Singh. Effect of quadratic radial variation of phase on single slit diffraction of laguerre-gauss vortex beams. *Journal of Modern Optics*, 59(14):1232-1242, 2012.

2. A. Ambuj, R. Vyas, and S. Singh. Diffraction of orbital angular momentum carrying optical beams by a circular aperture. *Optics Letters*, 39(19):5475-5478, Oct 2014.

Bibliography

[1] Francesco Maria Grimaldi. Physico mathesis de lumine, coloribus, et iride. *aliisque annexis libri duo*, pages 1–11, 1665.

[2] Thomas E. Woods. *How the Catholic Church built Western civilization*. Regnery Publishing, Washinton, D.C., 2005.

[3] Jordan Rigaud. *Correspondence of Scientific Men of the Seventeenth Century*, volume 2. Oxford University Press, Oxford, 1841.

[4] Thomas Young. The bakerian lecture: Experiments and calculations relative to physical optics. *Philosophical Transactions of the Royal Society of London*, 94:1–16, JAN 1 1804.

[5] A. Fresnel. Memoir on the diffraction of light. *Annales de chimie et de physique*, 11:246–296 and 337–378, 1819.

[6] Christiaan Huygens. *Treatise on Light*. Pieter van der Aa, Leiden, 1690.

[7] T.H. Maiman. Stimulated optical radiation in ruby. *Nature*, 187(4736):493–494, 1960.

[8] H. Kogelnik and T. Li. Laser beams and resonators. *Applied Optics*, 5(10):1550–1551, 1966 1966.

[9] A. E. Siegman. *Lasers*. University Science Books, Mill Valley, CA, 1986.

[10] Kazumasa Tanaka, Nobuhiro Saga, and Hiromu Mizokami. Field spread of a diffracted gaussian beam through a circular aperture. *Applied Optics*, 24(8):1102–1106, Apr 1985.

[11] Hal G. Kraus. Huygens-fresnel-kirchhoff wave-front diffraction formulation: paraxial and exact gaussian laser beams. *Journal of the Optical Society of America A*, 7(1):47–65, Jan 1990.

[12] Robert Brüning, Bienvenu Ndagano, Melanie McLaren, Siegmund Schröter, Jens Kobelke, Michael Duparre1, and Andrew Forbes. Data transmission with twisted light through a free-space to fiber optical communication link. *Journal of Optics*, 18(03), 2016.

[13] P. Török P. Varga. The gaussian wave solution of maxwell's equations and the validity of scalar wave approximation. *Optics Communications*, 152:108–118, 1998.

[14] M. W. Beijersbergen, L. Allen, H. E. L. O. Vanderveen, and J. P. Woerdman. Astigmatic laser mode converters and transfer of orbital angular-momentum. *Optics Communications*, 96(1-3):123–132, FEB 1 1993 1993.

[15] Anna T. O'Neil and Johannes Courtial. Mode transformations in terms of the constituent hermitegaussian or laguerregaussian modes and the variable-phase mode converter. *Optics Communications*, 181(1):35 – 45, 2000.

[16] N. R. Heckenberg, R. McDuff, C. P. Smith, and A. G. White. Generation of optical phase singularities by computer-generated holograms. *Optics Letters*, 17(3):221–223, Feb 1992.

[17] Queila S. Ferreira, Alcensio J. Jesus-Silva, Eduardo J. S. Fonseca, and Jandir M. Hickmann. Fraunhofer diffraction of light with orbital angular momentum by a slit. *Optics Letters*, 36(16):3106–3108, AUG 15 2011 2011.

[18] A. Ambuj, Hsiao harng Shiau, Michael Lucini, Reeta Vyas, and Surendra Singh. Effect of quadratic radial variation of phase on single slit diffraction of laguerre-gauss vortex beams. *Journal of Modern Optics*, 59(14):1232–1242, 2012.

[19] Devinder Pal Ghai, P. Senthilkumaran, and R. S. Sirohi. Single-slit diffraction of an optical beam with phase singularity. *Optics and Lasers in Engineering*, 47(1):123–126, JAN 2009 2009.

[20] J. M. Hickmann, E. J. S. Fonseca, W. C. Soares, and S. Chavez-Cerda. Unveiling a truncated optical lattice associated with a triangular aperture using light's orbital angular momentum. *Physical Review Letters*, 105(5):053904, JUL 29 2010 2010.

[21] Ashok Kumar, Pravin Vaity, and R. P. Singh. Diffraction characteristics of optical vortex passing through an aperture-iris diaphragm. *Optics Communications*, 283(21):4141–4145, NOV 1 2010 2010.

[22] A. Ambuj, R. Vyas, and S. Singh. Diffraction of orbital angular momentum carrying optical beams by a circular aperture. *Optics Letters*, 39(19):5475–5478, Oct 2014.

[23] John Vickers, Matt Burch, Reeta Vyas, and Surendra Singh. Phase and interference properties of optical vortex beams. *Journal of the Optical Society of America A*, 25(3):823–827, MAR 2008.

[24] H. He, N.R. Heckenberg, and H. Rubinsztein-Dunlop. Optical particle trapping with higher-order doughnut beams produced using high efficiency computer generated holograms. *Journal of Modern Optics*, 42(1):217–223, 1995.

[25] Joseph W. Goodman. *Introduction to Fourier optics*. McGraw-Hill, San Francisco, 1968.

[26] Max Born and Emil Wolf. *Principles of optics: electromagnetic theory of propagation, interference and diffraction of light*. Cambridge University Press, Cambridge, 2000.

[27] G. Goubau and F. Schwering. On the guided propagation of electromagnetic wave beams. *IRE Transactions on Antennas and Propagation*, 9(3):248–256, May 1961.

[28] G. Lenz. Far-field diffraction of truncated higher-order laguerre-gaussian beams. *Optics Communications*, 123(4-6):423–429, FEB 1 1996 1996.

[29] HI Sztul and RR Alfano. Double-slit interference with laguerre-gaussian beams. *Optics Letters*, 31(7):999–1001, APR 1 2006.

[30] I. Stegun M. Abramowitz. *Handbook of mathematical functions with formulas, graphs, and mathematical tables*. Dover Publications, New York, 1972.

[31] R. G. Paxman and J. R. Fienup. Optical misalignment sensing and image reconstruction using phase diversity. *Journal of the Optical Society of America A*, 5(6):914–923, 1988.

[32] G. B. Airy. On the diffraction of an object-glass with circular aperture. *Transactions of the Cambridge Philosophical Society*, 5:283–291, 1835.

[33] Ronald L. Phillips and Larry C. Andrews. Spot size and divergence for laguerre gaussian beams of any order. *Applied Optics*, 22(5):643–644, Mar 1983.

[34] J. Komrska. Fraunhofer diffraction at apertures in the form of regular polygons. i. *Optica Acta: International Journal of Optics*, 19(10):807–816, 10/01; 2014/05 1972.

[35] J. Komrska. Fraunhofer diffraction at apertures in the form of regular polygons. ii. *Optica Acta: International Journal of Optics*, 20(7):549–563, 07/01; 2014/05 1973.

[36] Anindya Ambuj, Reeta Vyas, and Surendra Singh. Diffraction of laguerre-gauss vortex beams by regular polygons. *Frontiers in Optics 2014*, page JTu3A.10, 2014.

[37] Hao Huang, Giovanni Milione, Martin P. J. Lavery, Guodong Xie, Yongxiong Ren, Yinwen Cao, Nisar Ahmed, Thien An Nguyen, Daniel A. Nolan, Ming-Jun Li, Moshe Tur, Robert R. Alfano, and Alan E. Willnerb. Mode division multiplexing using an orbital angular momentum mode sorter and mimo-dsp over a graded-index few-mode optical fibre. *Scientific Reports*, 5:14931, 2015.

[38] C. Allain and M. Cloitre. Optical diffraction on fractals. *Phys. Rev. B*, 33:3566–3569, Mar 1986.

[39] Jian Wang, Jeng-Yuan Yang, Irfan M. Fazal, Nisar Ahmed, Yan Yan, Hao Huang, Yongxiong Ren, Yang Yue, Samuel Dolinar, Moshe Tur, and Alan E. Willner. Terabit free-space data transmission employing orbital angular momentum multiplexing. *Nature Photonics*, 6:488–496, 2012.

[40] G. Gibson, J. Courtial, M.J. Padgett, M. Vasnetsov, V. Pas'ko, S.M. Barnett, and S. Franke-Arnold. Free-space information transfer using light beams carrying orbital angular momentum. *Optics Express*, 12:5448, 2004.

[41] F. J. Garcia-Vidal, L. Martin-Moreno, T. W. Ebbesen, and L. Kuipers. Light passing through subwavelength apertures. *Reviews of Modern Physics*, 82(1):729–787, Mar 2010.

[42] Darryl Naidoo, Filippus S. Roux, Angela Dudley, Igor Litvin, Bruno Piccirillo, Lorenzo Marrucci, and Andrew Forbes. Controlled generation of higher-order poincaré sphere beams from a laser. *Nature Photonics*, 10:327–332, 2016.

[43] Akihiko Ito, Yuichi Kozawa, and Shunichi Sato. Generation of hollow scalar and vector beams using a spot-defect mirror. *Journal of the Optical Society of America A*, 27(9):2072–2077, Sep 2010.

[44] Rupert F. Oulton, Volker J. Sorger, Thomas Zentgraf, Ren-Min Ma, Christopher Gladden, Lun Dai, Guy Bartal, and Xiang Zhang. Plasmon lasers at deep subwavelength scale. *Nature*, 461:629–632, 2009.

[45] Jeffrey N. Anker, W. Paige Hall, Olga Lyandres, Nilam C. Shah, Jing Zhao, and Richard P. Van Duyne. Biosensing with plasmonic nanosensors. *Nature Materials*, 7:442–453, 2008.

[46] H. He, M. E. J. Friese, N. R. Heckenberg, and H. Rubinsztein-Dunlop. Direct observation of transfer of angular momentum to absorptive particles from a laser beam with a phase singularity. *Phys. Rev. Lett.*, 75:826–829, Jul 1995.